JOURNAL OF GEOPHYSICAL RESEARCH, VOL. 107, NO. A7, 10.1029/2001JA900134, 2002

Return current region aurora: $\mathbf{E}_{\|}$, $\mathbf{j}_z$, particle energization, and broadband ELF wave activity

K. A. Lynch
Institute for the Study of Earth Oceans and Space, University of New Hampshire Durham, New Hampshire, USA

J. W. Bonnell and C. W. Carlson
Space Sciences Laboratory, University of California, Berkeley, California, USA

W. J. Peria
Geophysics Program, University of Washington, Seattle, Washington, USA

Received 19 February 2001; revised 19 June 2001; accepted 29 August 2001; published 19 July 2002.

[1] In this paper we consider ion heating in downward current, downward electric field, premidnight auroral regions. We show a case study, a test particle model, and a statistical study. The case study and statistical study use electron, ion, wave, and field-aligned current data and include wave spectra and ion pitch angle distributions. The ion pitch angle distribution functions are used to calculate, through the momentum balance equation, a self-consistent local parallel electric field. The test particle model shows ion pitch angle distributions and moments resulting from a "pressure-cooker" arrangement of magnetic and electric fields. This simple model can reproduce the ion pitch angle distributions and the moments of these distributions as seen in the statistical database; the parallel electric field calculated from these moments is consistent with the imposed electric field profile. The statistical database uses data from 23 premidnight auroral Fast Auroral Snapshot crossings. The statistical study shows that the ion to electron energy ratio varies from 1 to 10; the broadband ELF wave power is controlled by the local value of $\mathbf{j}_z \cdot \mathbf{E}_{\|}$; the relationship between $\mathbf{j}_z$ and $\mathbf{E}_{\|}$ is controlled by n_i; and the wave power near the cyclotron frequency is sufficient to provide the observed ion energies for oxygen in all cases and the observed ion energies for hydrogen for events near the poleward edge. The strong correlation between the wave power and $\mathbf{j}_z \cdot \mathbf{E}_{\|}$ validates the use of the ion distributions as a probe of the local $\mathbf{E}_{\|}$. As expected from theoretical arguments, the current-voltage relationship in these regions is seen to be controlled by the local ionospheric density. Allowing for suitable range in values of the density, the model can be applied to both strong return-current regions within the auroral cavity and weak-field regions at the poleward boundary. *INDEX TERMS:* 2409 Ionosphere: Current systems; 2704 Magnetospheric Physics: Auroral phenomena; 7867 Space Plasma Physics: Wave/particle interactions; *KEYWORDS:* Auroral Ionosphere, Auroral Electric Fields, Auroral Currents, Current-Voltage Relations, FAST Spacecraft, Auroral Particle Acceleration

1. Introduction

1.1. Pressure-Cooker Regions and Reverse Aurora

[2] In the auroral zone, electromagnetic and particle energy from the magnetosphere is transferred and transformed into heated ions, accelerated electrons, and waves. The auroral zone acts as an energy sink, a particle sink, and a particle source for the magnetosphere, absorbing electromagnetic energy via static current systems and dynamic Alfvén wave activity, and transforming that energy through a variety of well to marginally understood processes.

[3] In the canonical picture of an auroral arc (to the extent that one exists), an upward pointing DC electric field accelerates magnetospheric electrons down into the lower ionosphere, where they collisionally excite neutral atoms and generate light. On its way down, the precipitating electron beam excites a full spectrum of plasma waves from auroral kilometric radiation (AKR) and HF waves (megahertz frequencies), VLF whistler hiss (kilohertz frequencies), down to Alfvénic and ELF (below a kilohertz) oscillations. The ambient ionospheric plasma absorbs energy from these waves, and in particular, ions absorb energy transverse to **B**. As the ions increase their perpendicular energy, their magnetic moment gets pushed on by the magnetic mirror formed by the convergent magnetic field lines in the auroral zone. The ions move up as ion conics until they meet the original upward pointing DC field, where they are then accelerated outward into the magnetosphere. This canonical picture is very satisfying,

0148-0227/02/2001JA900134$09.00

and quite true as far as it goes. Inverted-V type arcs, as these canonical arcs are called, are a source region for upflowing ion beams; this has been known since Viking [*Lundin and Eliasson*, 1991], and clear examples of the formation of these beams are seen on Fast Auroral Snapshot (FAST) [*McFadden et al.*, 1998]. However, these beams are not the dominant source of ionospheric outflow to the magnetosphere. Sounding rocket measurements [*Bonnell et al.*, 1996; *Lynch et al.*, 1996; *Kintner et al.*, 1996] and statistical studies from Freja [*Norqvist et al.*, 1998; *André et al.*, 1998; *Knudsen et al.*, 1998] have shown that the dominant outflowing ionospheric ion populations are generally anticorrelated with the wave activity associated with inverted-V arcs (VLF whistler hiss.) Instead, the dominant ion outflow is found with the lower-frequency ELF and Alfvénic wave activity, historically associated with the edges of arcs and with shear and structure within arcs.

[4] One of the significant lessons learned from the FAST data set is an appreciation for the electrodynamic importance of what have been termed "inverse" aurora [*Carlson et al.*, 1998]. Glimpses of upgoing field-aligned electron beams were seen on Freja [*Marklund et al.*, 1994; *Boehm et al.*, 1995], but at Freja's 1700-km altitude the beams were generally weak and difficult to observe. The higher altitude of FAST and its excellent simultaneous coverage of both the upgoing and downgoing field-aligned directions allowed measurement of the prevalence of these upgoing electron beams. Virtually every auroral arc was found to have a "reverse" aurora partner. In these reverse arcs the upgoing electrons are broad in energy and highly field-aligned. It is exactly these regions that are the dominant source of outflowing ionospheric ions.

[5] The complication that makes the problem interesting is that in these regions (where the electrons are going out) the DC electric field is pointing the wrong way (as far as the outgoing ions are concerned.) The formation of the DC electric fields in reverse aurora is still under study [*Jasperse*, 1998; *Jasperse and Grossbard*, 2000; *Temerin and Carlson*, 1998], but there is clear experimental evidence for the divergent perpendicular electrostatic shocks consistent with downward pointing DC electric fields [*Ergun et al.*, 1998a]. The upgoing field-aligned electrons are thermalized field-aligned beams that originate by "falling" upward through a quasi-static potential drop. However, the DC field that pushes the electrons up also suppresses upgoing ions. This is the classical picture termed the "pressure-cooker" by *Gorney et al.* [1985]; the downward pointing field holds the ions down in the energization region until they acquire sufficient magnetic moment for their mirror force (upward) to overcome the DC electric field force (downward.)

1.2. Parallel Field Formation and Control

[6] The parallel electric fields that form in these regions must coexist with the accelerated electron and heated ion populations, and so the resulting electron and ion energization will affect the profile of the parallel field. The complementary problem within inverted-V regions has been solved theoretically [*Alfvén and Falthammar*, 1963], but this quantitative feedback loop is still under study in regions of downward current. Qualitative and numerical solutions exist [*Jasperse*, 1998; *Jasperse and Grossbard*, 2000; *Temerin and Carlson*, 1998], showing that the self-consistent $\mathbf{E}_{\|}$ is necessarily negative for downward current regions when quasi-neutrality is strictly enforced. However, a fully self-consistent solution is difficult because of the strong interdependence of the externally demanded current, the ionospheric and plasma sheet densities and temperatures, and the electron and ion energization that develop from the resulting electric field and wave activity.

[7] In the theoretical description presented by *Temerin and Carlson* [1998] these regions are delineated and controlled by an externally applied field-aligned current requirement. The demand for current along the field line, although at first glance easily met by the ionospheric densities, is actually severely limited by the ion density along the flux tube and the requirement for charge neutrality. To keep the electron density low but the current high, high electron velocities are required, and therefore a potential drop must form. The current-voltage relation in this region is a complicated function of the densities and temperatures of all the different populations along the field line: ionospheric ions and electrons, as well as magnetospheric ions and electrons. Then, since the parallel field formation has effects on the ionospheric populations (i.e., ion heating and electron beams), there are strong feedbacks which must be part of any complete model. We will see below that the coexistence of the downward current and the downward electric field results in energy dissipation that is divided between the electron acceleration, the electron beam thermalization, wave generation, and ion heating.

[8] In this paper we show statistics from FAST data that can be used to parameterize and restrict this problem. Previous statistical studies from other spacecraft have examined altitude dependences of ion conics (Akebono) [*Miyake et al.*, 1993] and wave-particle interactions of transverse ion acceleration (Freja) [*Norqvist et al.*, 1998]. In our study we include a new technique based on theoretical work presented by *Jasperse and Grossbard* [2000]: we use the moments of the ion data phase space distribution functions to calculate a self-consistent local parallel electric field. We use this measure of the local electric field, $\mathbf{E}_{\|}^{i}$, to examine the relationships between the large-scale energy inputs ($\mathbf{j}_z \cdot \mathbf{E}_{\|}$) and the microphysical dissipation and energization processes: broadband ELF activity and ion conic development.

1.3. Broadband ELF Literature and Questions

[9] Since broadband ELF (BBELF) wave activity is believed to be responsible for the perpendicular ion acceleration in these regions, an understanding of its detailed properties is necessary in order to understand how it might interact with the ions and how it might act as an energy conduit between the streaming electron distribution and the ion conics. We do not yet fully understand the relationship between the different ion and electron distributions and the BBELF wave activity, but some features are obvious. Previous observations and theory indicate that parallel electron drift provides most of the free energy for such waves [*Cattell et al.*, 1998; *Bonnell et al.*, 1996; *Kindel and Kennel*, 1971]. The most energetic ion conics are also usually coincident with broadband enhancements in the wave power, as reported by *André et al.* [1998], and a more detailed analysis of the

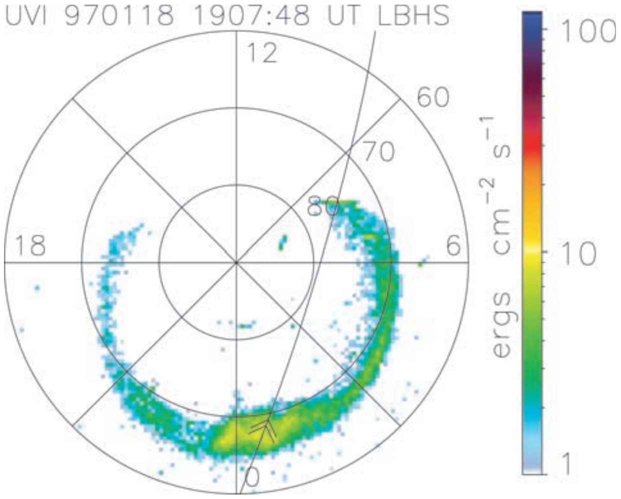

Figure 1. The location of Fast Auroral Snapshot (FAST) and its trajectory with respect to the arc system during our example event, as seen by the Polar Ultraviolet Imager (UVI) instrument. Courtesy of the University of Washington, Geophysics Program, G. K. Parks.

BBELF and its interaction with the ions is warranted. We will show below that BBELF can be either featureless and broadband or can show cyclotron-frequency structuring. A case study (C. Chaston, private communication, 2000) found that the electron drift is higher in the broadband enhancements than in the cyclotron-structured intervals, in agreement with a linear instability analysis. This suggests that further linear analysis will shed light on the nature of the instability that produces the BBELF, as well as the details of the energy transfer from the parallel electric field to the streaming electrons, through the waves, and finally into the ion conics. Linear analysis should also shed light on how much, if any, of the wave activity is driven by the unstable features in the conics themselves and how much is driven by the interaction between the conics and the streaming electrons.

[10] Regardless of the exact nature of the BBELF itself, strong correlations between its presence and both ion heating and parallel energy dissipation exist, as we show in this study and as has been reported elsewhere [*André et al.*, 1998; *Lynch et al.*, 1996; *Bonnell et al.*, 1996]. In this paper we show statistical results parameterizing the relationship between the BBELF wave activity and the accompanying particle and field data.

1.4. Outline

[11] The outline of the paper is as follows. First we show a case study of an example "pressure-cooker" region in a premidnight auroral crossing and describe the characteristic signatures in the electron, ion, current, and wave field data. Then we review a theoretical description of the relationship between the parallel electric field and the ion phase space distribution patterns in these regions. We present a simple test particle model of ion motion in a downward electric field, converging magnetic field geometry, in order to illustrate expected particle behavior in these regions. In the second half of the paper we present statistical data from 23 FAST crossings of premidnight aurora. We conclude with discussions of energy flux, causality, and wave activity in these "reverse aurora" regions.

2. Case Study: FAST Orbit 1626

[12] Let us consider a typical example of one of these regions as seen by the FAST instrumentation. We will show the particle and field data as a function of time, as well as details of the wave data. Then we study the various shapes of ion distribution functions seen throughout the event and, for comparison, seen in other regions such as inverted-Vs.

2.1. Survey Versus Time

[13] Figure 1 shows the trajectory of the FAST spacecraft into the arc at the time of interest, superposed on a Polar spacecraft Ultraviolet Imager (UVI) image of the auroral zone. The trajectory crosses poleward into the arc at close to normal incidence, and 1907:48 UT, the time of the image, is the center of the time interval of the case study shown in Figure 2. Figure 2 shows the in situ observations. On the

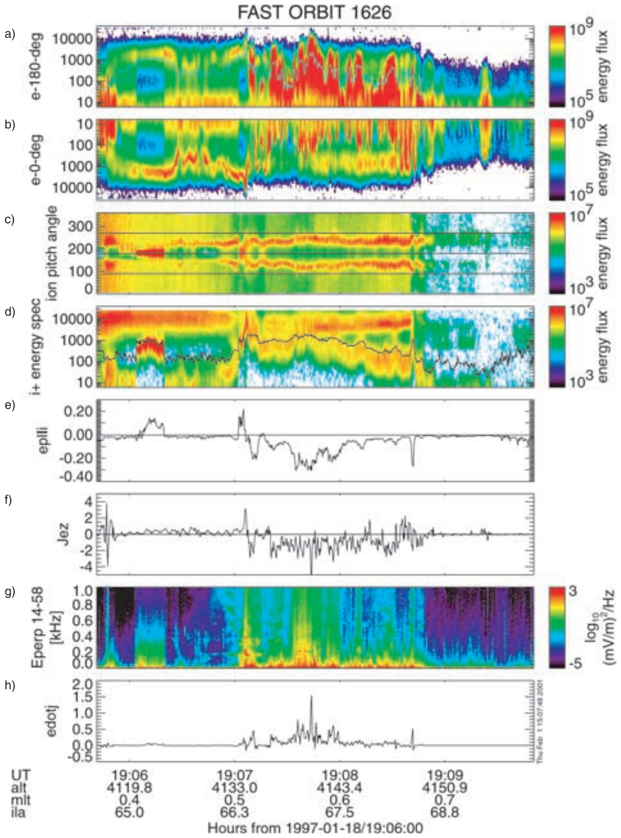

Figure 2. Data for the example event (all energies are in eV): (a) upgoing electrons; (b) downgoing electrons (note reversed energy axis); (c) ion pitch angle spectra (all energies); (d) ion energy spectra (all pitch angles); (e) the parallel electric field computed from the ion distributions, $\mathbf{E}_{\parallel}^{i}$ (mV/m); (f) upward current (μA m^{-2}) carried by the measured electrons (current is positive upward, negative for upgoing electrons, in this convention); (g) ELF spectrogram from the 14–58 channel; (h) $\mathbf{E}_{\parallel}^{i} \cdot \mathbf{j}_{z}^{e-}$ (mV m^{-1} $\times$ μA m^{-2}). The altitude of the observations shown varies from 4100 to 4150 km, the invariant latitude is near 67°, and the magnetic local time is near midnight.

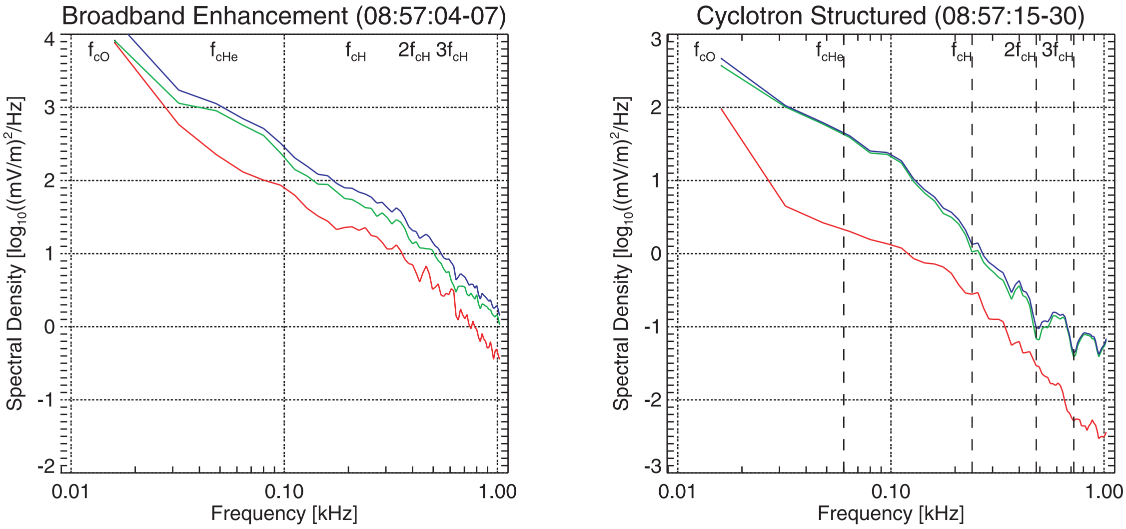

Figure 3. Examples of parallel and perpendicular electric field spectra for (left) broadband enhancements and (right) cyclotron-structured lower-intensity intervals. The blue, red, and green lines are the total, parallel, and perpendicular spectral densities in the spin plane. Ion cyclotron frequencies and harmonics are indicated by dashed lines.

equatorward side (1906–1907 UT) there is a large inverted-V structure marked by downgoing electrons (Figure 2b, note inverted energy axis) and upward current (Figure 2f). There are some ion conics there (Figure 2c), but they are weak in energy and flux. There are also two ion beams, at 1906:10 and at 1907 UT. Just poleward of the inverted-V, there is a strong return-current-region, or "reverse" aurora. This region is indicated by upgoing electrons (Figure 2a), downward current (Figure 2f), energetic ion conics (Figure 2c), and strong, broadband ELF activity (Figure 2g). The higher-energy (10 keV) precipitating ion fluxes that are evident here are always seen in these regions as well, making these ion conics similar to the "Type 2" conics described by *André et al.* [1998]. The conics in this region typically have $T_\perp$ to $T_\parallel$ ratios of $\sim$3, ranging as high as 9 in some places.

[14] Figures 2e and 2h show calculations of parallel electric field inferred from the ion moments, $\mathbf{E}^i_\parallel$, and of energy dissipation, $\mathbf{j}_z \cdot \mathbf{E}_\parallel$. These panels will be discussed in section 3.

[15] The interval from 1907 to 1908:40 UT is a classic example of the "pressure-cooker" ion heating scenario described by *Gorney et al.* [1985]. The upgoing electrons, which are strongly field-aligned, are consistent with acceleration of cold ionospheric electrons by an earthward pointing DC electric field. The broad energy spectrum and occasional counter streaming of these field-aligned electrons are consistent with a strong field-aligned thermalization process; though there is a peak in the differential energy flux spectrum as shown here, a plot in phase space density typically shows a broad plateau extending down from the upgoing peak energy and into the downgoing direction [*Carlson et al.*, 1998]. The earthward pointing DC electric field that is inferred from the electron data, is then retarding the upward motion of the ion conics. For ions to have reached the altitude of the observation, they must have acquired sufficient transverse energy to overcome the altitude-dependent electric field via the mirror force. This energy filter effect is seen clearly in Figure 2d, from 1907:10 to 1908:40 UT; there is a clear minimum energy in the ion spectrum, below which there are very few counts. Note that this low-energy minimum in the ion count rate is not due to the usual fall of detector count rate with decreasing energy but instead represents a true dearth of phase space density at low energies in the ions.

2.2. BBELF Structure

[16] The BBELF wave activity during the case study event, shown in Figure 2g, is coincident in time with upgoing electron fluxes and high-energy ion conics. Typically in return current regions, we can see two types of electric field spectra: (1) broadband enhancements without strong structuring at multiples of f_{cH} and (2) relatively weaker enhancements with nulls at multiples of f_{cH}. Both types of spectra also include a smooth higher-power portion extending below f_{cH}. There is often no clear evidence during these intervals for the strong, nonlinear wave activity and ion acceleration represented by fast solitary structures [*Ergun et al.*, 1998b], so a local, linear analysis of the waves can allow us to understand how the waves are generated and how they interact with the ion conics.

[17] We can examine more carefully the spectral shapes of the BBELF within return current regions. Figure 3 shows examples of both broadband enhancements and weaker enhancements with nulls at multiples of f_{cH}, taken from a different case study. (While the data shown in Figure 2 include examples of both broadband and structured spectra, the two types are not well-distinguished in that particular example.) In the left panel of Figure 3, an example of a broadband enhancement, the ratio of parallel to perpendicular spectral densities is $\sim$1/3, and the spectra have no obvious structures ordered by f_{cH}.

[18] The waves during the cyclotron-structured intervals are weaker, by about a factor of 10 in total power, as can be seen in the right panel of Figure 3, and the ratio of parallel to perpendicular spectral density is about 1/10; that is, the

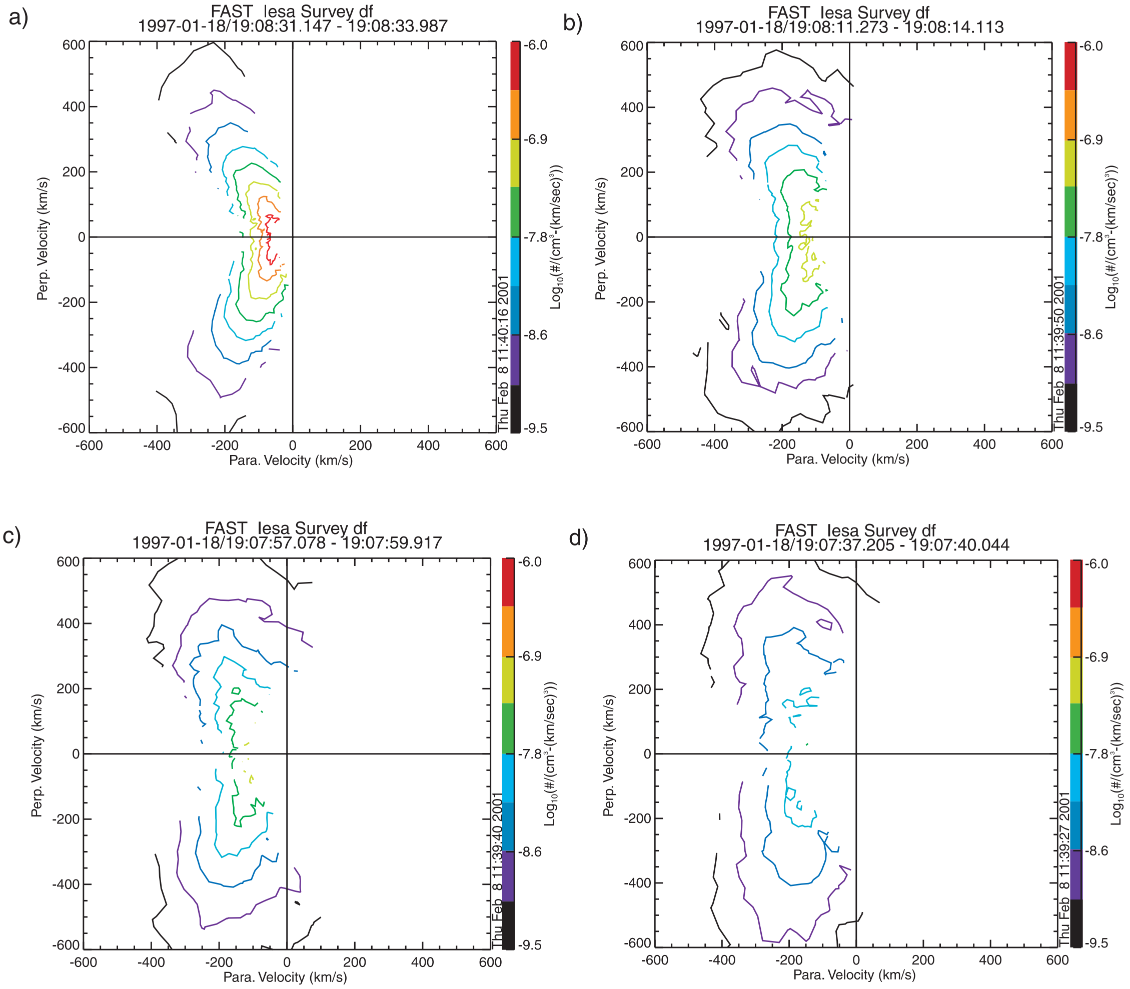

Figure 4. (a–d) Ion distribution function contours as functions of $v_\perp$ and $v_\|$, during the event shown in Figure 2. The UT time of each example is given in the title. Distribution functions are integrated over eight survey data distribution functions (2.8 or 5.6 s, depending on instrument mode), and a floor of four counts per interval is used to cut off the contouring. Mass is assumed to be hydrogen.

cyclotron structured waves are more perpendicularly polarized. One can also see depletions in the perpendicular spectral density at $2f_{cH}$ and $3f_{cH}$, similar to that observed in previous case studies [*Ergun et al.*, 1998a].

[19] The lack of nulls at $n \cdot f_{cH}$ in the broadband case, as well as the missing null at f_{cH} in the cyclotron-structured case, indicates relatively weak damping of the waves by ions, suggesting that the ions are inefficiently removing energy from the waves or that the energy may not be transferred via a cyclotron resonance. The gyroresonant heating model [*Chang et al.*, 1986] predicts the maximum possible H^+ heating rate of 960 eV s^{-1} for the broadband spectrum, an overestimate given the moderate ion energies (1 keV) and oblique pitch angles of the ion distribution at the time of this example. The maximum heating rate during the cyclotron-structured interval is 24 eV s^{-1}, which is more in line with the few hundred eV conic energy during that interval.

2.3. Ion Phase Space Distribution Patterns

[20] Consider now the ion distribution function patterns during this example, shown in Figure 4. Even across this 90-s interval, there is a rich variety in the ion conic structures. At the end of the conic interval (Figure 4a), the distribution has a fairly well-defined pitch angle and not much upward drift. There is, however, strong diffusion as can be seen by the filled-in plateaus between the arms of the conic. Moving into the pressure-cooker region (backward in UT), the apex of the conic moves upward off the $v_\| = 0$ axis (Figure 4b). The pitch angle becomes less well defined, roughly increasing with energy, and the perpendicular diffusion signature becomes stronger.

[21] Where the waves are most intense, the distribution (Figure 4c) shows strong perpendicular diffusion, but since $v_\|$ is nonzero, the entire structure is lifted upward. Finally, Figure 4d shows a strong pressure-cooker signature, with perpendicular diffusion from the heating, parallel diffusion from the electric field precipitating some of the particles, an overall lifted apex, and a large $T_\|$. The spread in parallel ion velocity associated with $T_\|$ comes from the parallel motion of ions that have temporarily lost energy and are moving downward in response to $\mathbf{E}_\|$ (see discussion in section 4). The signature of these precipitating particles can be seen in the $v_\| > 0$ hemisphere of the third and fourth examples.

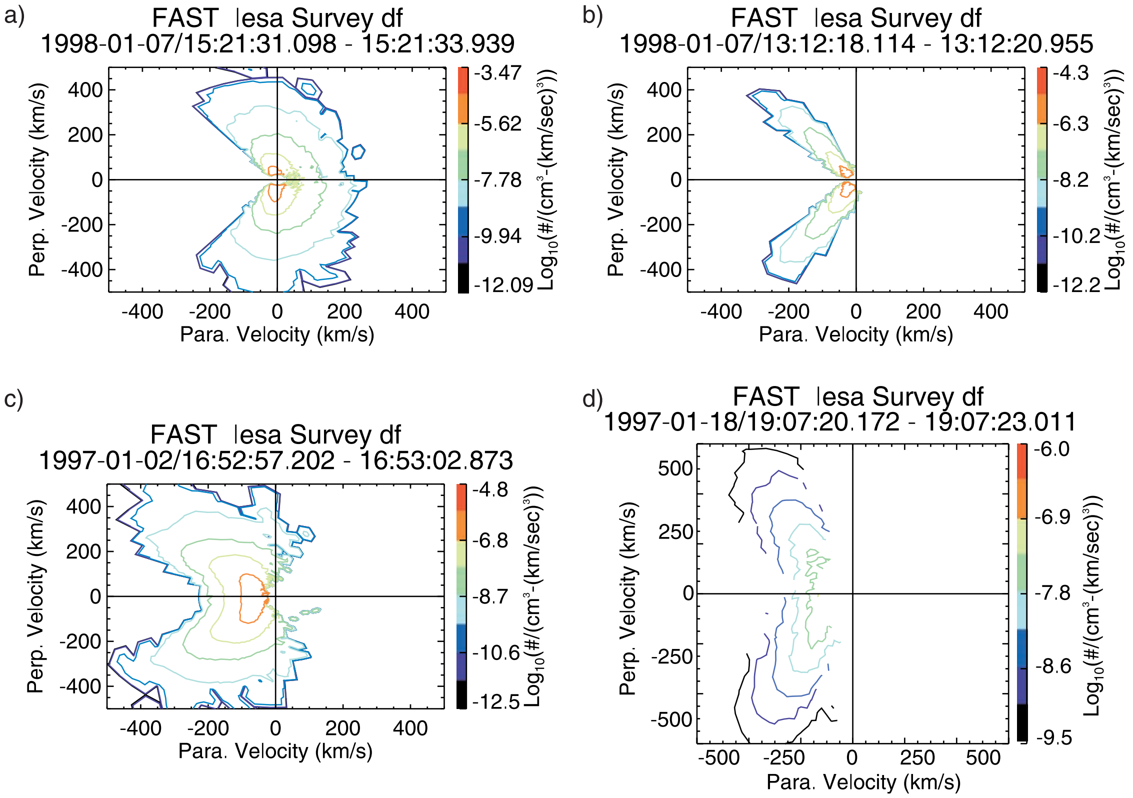

Figure 5. Ion distribution function contours as functions of $v_\perp$ and $v_\parallel$, taken from various premidnight auroral conditions: (a) low altitude, (b) inverted-V, (c) oscillating electron flux region, and (d) nongyrotropic example. Format is as in Figure 4.

[22] For further illustration of the variety of conics which can be seen, Figure 5 shows distribution patterns from a very low altitude observation, from an inverted-V region, from a region with oscillating upward and downward electron fluxes, and from an example that is nongyrotropic. All of these examples come from midnight or premidnight local times, at altitudes within the 2000–4000 km range of FAST observations. The low-altitude observation (Figure 5a) shows the type of conic first described by Gorney's 1985 model, where there is a significant component of the conic population in the downgoing direction. The inverted-V region conic (Figure 5b) is quite different from all the others, as it has a narrowly defined pitch angle width and its apex is firmly mounted at the origin. Figure 5c shows a conic at the extreme poleward edge of an arc, near a sudden change in the electron bulk flow direction from upward to downward. Figure 5d shows an example of the fairly common nongyrotropy of strong pressure-cooker ion conics. This particular example is taken from the case study shown in Figure 2.

3. Theory of Ion Phase Space Distribution Structure and $E_\parallel$ Formation in Downward $E_\parallel$ Regions

[23] As a result of the complicated field morphology in these regions, the shape of the ion conic distribution functions can contain valuable information about the parallel electric field on a given flux tube. *Jasperse and Grossbard* [2000] derive the parallel electric field that is consistent with an observed particle distribution function in a dipolar magnetic field. The steady state kinetic diffusion equation in one space and two velocity space dimensions, plus a quasi-neutrality condition, yields an equation for momentum balance:

$$\frac{d}{ds}\left(n_\alpha w_{\alpha\parallel}\right) - \frac{1}{B}\frac{dB}{ds}n_\alpha\left(w_{\alpha\parallel} - \frac{1}{2}w_{\alpha\perp}\right) + \frac{1}{2}n_\alpha q_\alpha \frac{d}{ds}\Phi_{\alpha\parallel} = 0,$$

which can be recast as (given that $(d/ds)\,\Phi = -E_\parallel$ and s is distance along the field line)

$$E_\parallel = \frac{2}{q_\alpha}\left[\frac{1}{B}\frac{dB}{ds}\left(\frac{1}{2}w_{\alpha\perp} - w_{\alpha\parallel}\right) + \frac{1}{n_\alpha}\frac{d}{ds}n_\alpha w_{\alpha\parallel}\right].$$

Here the w are the perpendicular and parallel energy moments of the species α; that is, $w_\perp = T_\perp$ and $w_\parallel = (1/2)T_\parallel + (1/2)mu_\parallel^2$. While, in principle, the quantity $\mathbf{E}_\parallel$ must be the same for all species (all the species must be consistent with a given parallel field), we will use the notation $\mathbf{E}_\parallel^i$ to remind the reader that our measure of the parallel field is derived from the ion data.

[24] A theoretical model of the parallel electric field along the flux tube requires the self-consistent solution of this and other moment balance equations (number flux, energy flux, and closure relations). An analytical solution of this system has been found for upward-current systems (the

Alfvén-Falthammar formula [*Alfvén and Falthammar*, 1963]) but analytic solutions for downward-current systems are still being studied [*Jasperse and Grossbard*, 2000; *Jasperse*, 1998; *Temerin and Carlson*, 1998]. The modeling requires knowledge of the ion heating rate $d(w_{\alpha\perp})/dt$, which enters on the right-hand side of the higher moment balance equations and which accumulates to give the value of $w_{\alpha\perp}$. However, for our purposes right now, we can use the observed values of $w_{\alpha\perp}$ and $w_{\alpha\parallel}$ to infer the parallel electric field that is consistent with the observed ion phase space distributions at the point of observation. To do this, we need to neglect the pressure gradient term, $(1/n_\alpha)d(n_\alpha w_{\alpha\parallel})/ds$. This (upward) ambipolar field is generally small compared to the larger downward field term, though it can reach as high as 25% [*Jasperse and Grossbard*, 2000].

[25] Figure 2e shows the results of this calculation for our case study event. The moments of the ion data for energies below 3 keV (to exclude high-energy ion precipitation) are calculated and used to infer a parallel electric field as shown above. In the regions where the field-aligned current is negative (upgoing electrons), the inferred parallel field is mostly negative and corresponds to the ion energy and wave activity. Similarly, in the inverted-V region, when the spacecraft moves into the local upward parallel electric field as evidenced by the ion beams, the $\mathbf{E}_\parallel^i$ signature is large and positive. Note that because of the 3-keV energy break in the ion calculations, the ion beam is not fully included in this calculation, so $\mathbf{E}_\parallel^i$ is quantitatively incorrect in the second ion beam example (near 1907 UT). However, the sign and rough magnitude are indicative of the upward parallel fields here.

[26] In particular, we can examine the parallel field consistent with each of the ion distributions shown in Figures 4 and 5. Figures 4a–4d are distributions consistent with a steadily increasing parallel field: (Figure 4a) −0.05, (Figure 4b) −0.1, (Figure 4c) −0.2, and (Figure 4d) −0.3 mV/m (note that the sequence moves backward in UT.) Figures 5a–5d are consistent with: (Figure 5a) −0.025, a low value at the bottom of a parallel field altitude profile, (Figure 5b) −0.02, an nonfield (below inverted-V) region, (Figure 5c) −0.015, a polar cap edge region where the electron flux is moving up and down, and (Figure 5d) −0.1 mV m^{-1}, a nongyrotropic example at the edge of a strong pressure-cooker region.

[27] Note the relationship between the quantity $\mathbf{j}_z^{e-} \cdot \mathbf{E}_\parallel^i$ and the broadband ELF intensity, both in the return current region and in the ion beam region where both $\mathbf{J}_z$ and $\mathbf{E}_\parallel$ are reversed. Figure 2h shows $\mathbf{j}_z^{e-} \cdot \mathbf{E}_\parallel^i$ as a function of time. Figure 6 illustrates the very good correlation between $\mathbf{j}_z^{e-} \cdot \mathbf{E}_\parallel^i$ and the BBELF wave power at the oxygen cyclotron frequency. In part, this serves as a validation of our use of the ion data as a prove of the local parallel field; here $\mathbf{j}_z^{e-}$ is derived from the electron data, $\mathbf{E}_\parallel^i$ is derived from the ion data, and spectral density is derived from the field data. There is no instrumental reason why they should be correlated, yet the correlation factor is better than 0.8, as would be expected when comparing a measure of power input ($\mathbf{j}_z^{e-} \cdot \mathbf{E}_\parallel^i$) with a measure of dissipation (wave spectral density.) We will return to these comparisons in section 5.

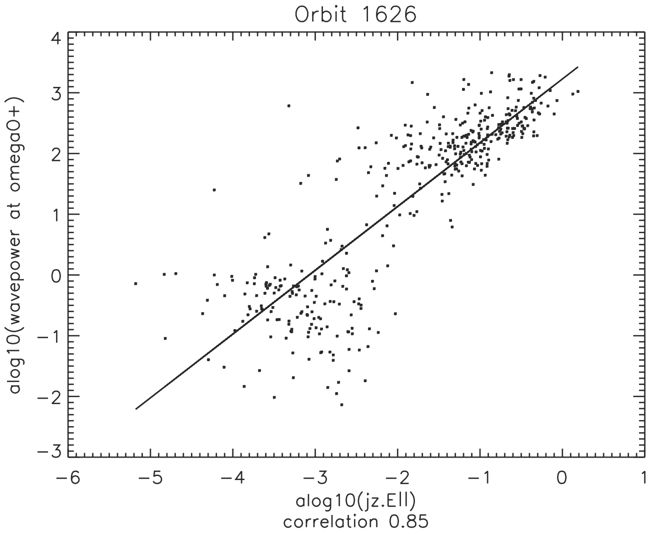

Figure 6. Correlation between $\mathbf{j}_z^{e-} \cdot \mathbf{E}_\parallel^i$ and broadband ELF wave power at Ω_{O^+}, for data from the example shown in Figure 2. The correlation factor is 0.85.

[28] Note that $\mathbf{E}_\parallel^i$ provides a probe of the local parallel electric field, unlike observations of the upgoing electron energy [*Carlson et al.*, 1998; *Ergun et al.*, 1998a], which provide information on the integrated parallel field below the observation, or the potential drop. (The electron characteristic energy, J_E/J, is equal to e times the potential drop below the observation point [*Jasperse and Grossbard*, 2000].) The two different observations together can be used to constrain the properties of the parallel field in the return current regions. An interesting point to note is that the lifetime of the ion conic on a flux tube can be over 100 s, while the transit time for an accelerated electron can be less than 1 s. Thus the electron data reflect the near-instantaneous behavior of $\Phi_\parallel$, while the ion data reflect the integrated recent history of $\mathbf{E}_\parallel$ along the flux tube. Thus the fact that the electron energies tend to vary much more rapidly than the ion energies can be used to infer the time evolution of the parallel fields, as will be discussed in section 4.

4. Model of Ion Energization and Phase Space Distribution Structure in Downward $\mathbf{E}_\parallel$ Regions

[29] Many aspects of the ion behavior in downward $\mathbf{E}_\parallel$ regions can be understood through a test particle model of the effects of the earthward pointing DC $\mathbf{E}$ field, the upward pointing mirror force, and the transverse acceleration of ions via waves [*Gorney et al.*, 1985]. The motion of the gyrocenter of an ion in the converging auroral $\mathbf{B}$ field lines can be written as a closed set of ordinary differential equations. The equation of motion for velocity along the field line includes the acceleration from the parallel field as well as from the mirror force:

$$m\frac{dv_\parallel}{dt} = eE_\parallel - w_\perp \frac{1}{B}\frac{dB}{dz},$$

where $\mathbf{B}(z)$ is given by a dipole field altitude dependence and $w_\perp$ is the particle's transverse energy. The equation of motion for the perpendicular component of velocity includes a transverse heating term (wave-particle interaction) as well as the mirror force:

$$\frac{dw_\perp}{dt} = v_\parallel w_\perp \frac{1}{B}\frac{dB}{dz} + \left(\frac{dw_\perp}{dt}\right)_{\mathrm{WPI}}.$$

The third equation is the motion along the field, $dz/dt = v_\parallel$. The particle motion then can be computed as a function of $v_\parallel$, $v_\perp$, and z:

$$\frac{dv_\parallel}{dt} = e \cdot E_\parallel / m + 3 \times 0.5 v_\perp^2/(R_e + h),$$

$$\frac{dv_\perp^2}{dt} = -3 v_\parallel v_\perp^2/(R_e + h) + \frac{2}{m}\left(\frac{dw_\perp}{dt}\right)_{\mathrm{WPI}},$$

$$\frac{dz}{dt} = v_\parallel.$$

[30] In the original application of this model, to high-altitude day side heating from cyclotron wave activity, the perpendicular heating rate was parameterized as a single constant value. In our present application the perpendicular energization is presumed to come from a series of random perpendicular velocity "kicks" from the interaction of the ions with the broadband ELF wave activity. This interaction can be modeled by choosing, at each time step, a perpendicular delta velocity from a normal distribution, vector-adding it to the ion's velocity at that time step, and calculating the change in perpendicular energy from that kick (which can be either negative or positive.) Similar calculations have been made in other models [*Temerin et al.*, 1986; *Hultqvist*, 1996].

[31] Reproducing the ion conic distribution function data then becomes a matter of choosing altitude profiles of the electric field and ion energization. Constraints on these choices are found in (1) the electron data, which indicate the value of the integrated parallel electric field up to the observation altitude; (2) the ion data, both energy and pitch angle distribution, which constrain the allowed values of the electric field; and (3) reasonable assumptions about the possible efficiency of the wave-particle interaction between the ions and the BBELF (broadband ELF).

[32] A limitation of this simple model is that the electric field profile is imposed, rather than being developed self-consistently with the particle and field populations [*Jasperse and Grossbard*, 2000]. However, we can use this simple model to probe the parameter space of possible electric field profiles to find the patterns that best reproduce the data. The ion and electron data, taken together, constrain both the total potential drop and the maximum electric field value and thus guide the choice of the extent and shape of the parallel field profile. The ion distributions then can be used to calculate the electric field with which they are consistent as discussed in section 3, which can then be compared to the input electric field profile for consistency.

[33] The first choice was made by noting that for a majority of the ion distribution functions seen in the regions under study, the dominant parallel velocity was upward (see Figure 4). Except at low altitudes, the conics are "lifted"; that is, they have an upshifted conic apex. This constrains the electric field profile considerably, as a "typical Gorney model" conic generally has a downflowing component at small $v_\perp$ [*Jasperse*, 1998]. We ran the model "in reverse," as it were, choosing a value for $\mathbf{E}_\parallel$ at each time step that generated a small positive value for $dv_\parallel$, and then plotted the resulting parallel field altitude profile. An example is shown in Figure 7a. The result was reassuringly similar in shape to the self-consistent parallel fields generated by the more rigorous model *Jasperse and Grossbard* [2000] and *Jasperse* [1998]. The difference between this choice and a simple step function or linear ramp comes down to the curve at the bottom, which allows the electric field to grow as quickly as possible with altitude without precipitating most of the ambient ions that enter from below. (Note that quasi-neutrality requires just such a situation to develop: if all the ions are precipitated, no electron current can flow.) The overall amplitude of the parallel field can then be chosen to match a given choice of potential drop, i.e., to match an electron energy spectrum at observed altitudes.

[34] Next, a profile of heating rate must be chosen. For arguments discussed in section 5 we chose a heating profile that was linearly proportional to the local parallel electric field. Briefly, this is because the wave power is observed to be proportional to $\mathbf{j}_z \cdot \mathbf{E}_\parallel$. For a given $\mathbf{j}_z$, then, the wave energy density should be proportional to the parallel electric field; if the heating rate is proportional to the wave energy density, then the heating rate has the same altitude profile, for a fixed $\mathbf{j}_z$, as the parallel field. (Note that this introduces some inconsistency as $\mathbf{j}_z$ should vary with $B(z)$.) The overall amplitude of the heating rate profile was then chosen by running the model for a given parallel electric field profile and then varying the heating rate amplitude until temperature ratios matching those of the statistical database were produced.

[35] Figure 7 shows the results of these choices for a run that would produce 100-eV electrons at 4200-km altitude. Figure 7a shows the altitude profile of the parallel electric field; the diamonds show the electric field inferred from the resulting ion distributions as discussed above. The heating profile is proportional to the electric field profile, and maximizes at a value of 50 eV s^{-1}. Figures 7d–7f show the resulting ion distribution functions at three different altitudes. Note the change in axes in Figure 7f. Figure 7d, the low-altitude distribution, shows the beginnings of the ion conic overlaid with higher-energy precipitation. This precipitation is from ions at higher altitudes getting random kicks that reduce their perpendicular energy and are then precipitated by the electric field. Figure 7e, at midaltitudes, shows how the random perpendicular acceleration results in fairly strong parallel diffusion as well. Figure 7f shows the mirror force forcing the conic upward in pitch angle. Figures 7b and 7c show moments of these distributions; the bulk drift velocity (here plotted as velocity parallel to **B**, so negative is upward) increases with altitude to ~100 km s^{-1} above 4000 km, and the ratio of perpendicular to parallel temperature maximizes at only ~25, because of the strong parallel diffusion.

[36] The moments of the distributions (v_i, $T_\perp$, $T_\parallel$) are combined to calculate the inferred electric field consistent with these distributions; this is shown by the diamonds in

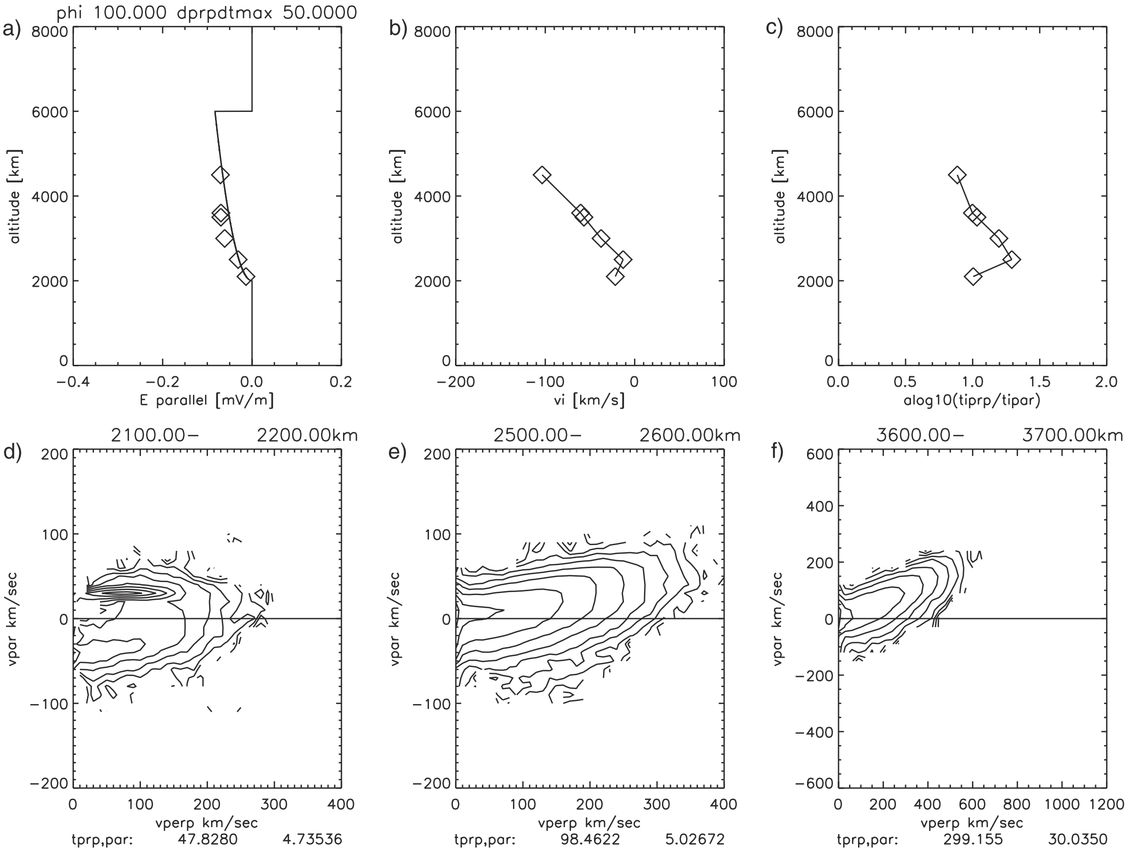

Figure 7. Results of test particle model: (a) input $E_{||}$, (b, c) resulting flow and temperature moments, versus altitude, and (d–f) resulting ion distributions at different altitudes.

Figure 7a. The agreement is reasonable but not perfect; the distributions infer an electric field nearly 50% greater than that imposed at 2500 km but match fairly well near the top and bottom of the profile. The entire example scales with the overall potential drop; if the potential drop is set at x volts and the maximum heating rate is set at $x/2$ eV s^{-1}, with the same profile shapes as shown, similar distribution function shapes are reproduced at higher or lower energies, depending on the value of x. A model output that can be compared interestingly to the statistical database results is the ratio of ion energy to electron energy at any given spot. The ion energy (kinetic plus thermal) is generally 5–10 times that of the collocated electron (characteristic) energy and is considerably more than that near the bottom of the electric field structure. We note in passing that it is interesting to consider what happens to this ratio if we allow the electric field and potential drop magnitude to vary with time, since the ion and electron transit times through the region are so different. For enforced electric field profiles that vary on timescales similar to the ion transit time, the average ion to electron energy ratio drops considerably and has a rather different altitude profile. We will return to this point in section 6.

5. Statistical Data

5.1. Statistical Database

[37] FAST satellite data from 23 nightside auroral crossings were used to build the statistical database. Figure 8 shows the range of magnetic local time, invariant latitude, altitude, and distance from the polar cap edge, covered by the data. The time resolution of the data used in the statistics is that of one distribution function from the particle detector survey data, typically a fraction of a second. The database includes 18,060 sample times, of which 3416 meet the "good data" conditions described below and are used in the statistics. Orbit numbers used were as follows: 1526, 1569, 1580, 1600, 1601, 1633, 1720, 1731, 1750, 1766, 1782, 1799, 1822, 1959, 5448, 5450, 5451, 5453, 5454, 5472, 5506, 5572, and 5599.

[38] The data quantities that make up the database can be grouped into four classifications: morphology, particle moments, field-aligned current, and BBELF quantities. The morphological quantities are universal time, altitude in kilometers, magnetic local time, invariant latitude, and δ_{ILAT}, or equatorward distance from the polar cap edge in degrees of invariant latitude. The altitude range of the data extends from 2030 to 4156 km. The magnetic local time, which was used as a selection criterion for events, ranges from 2000 to 0200. Enough passes were used to avoid clear MLT-ALT biases, although there is a prevalence of high-altitude (above 3500 km) events. The δ_{ILAT} quantity is based on a manual determination of the invariant latitude of the poleward boundary of the auroral oval using electron data. This evaluation is reproducible to usually better than 0.5° in latitude. For one or two passes that cross the auroral zone in a glancing manner, this quantity is not clear and is left undefined; data from

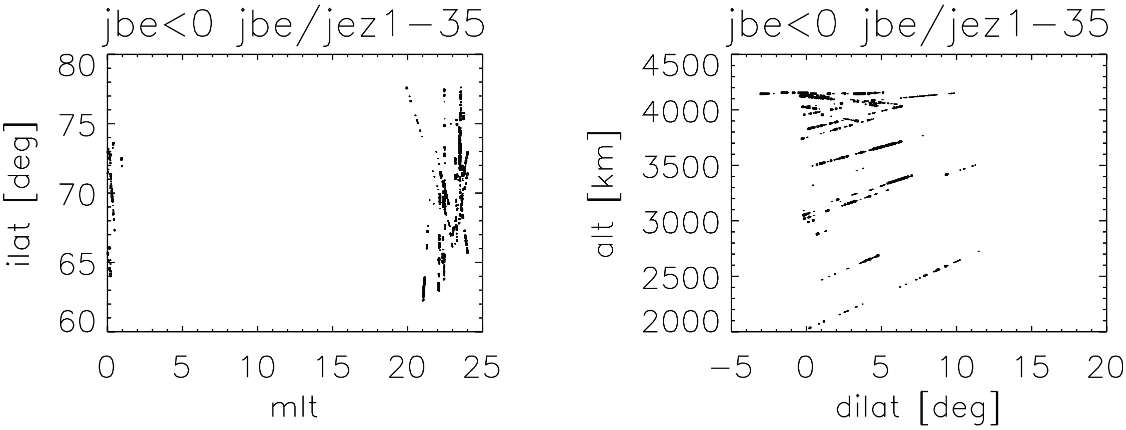

Figure 8. Distribution of statistical event data in (left) magnetic local time (MLT) versus invariant latitude (INVLAT) and (right) distance from polar cap edge versus altitude. Data are from 23 auroral zone passes. A total of 3416 points meet the conditions that $\mathbf{j}_z^B$ is negative and that $\mathbf{j}_z^B/\mathbf{j}_z^{e-}$ is greater than 1 and less than 35. Highlighted points (982) are further restricted by the condition that the particle moments give upgoing ion and electron energy fluxes.

these passes are not used in plots that show data as a function of δ_{ILAT}.

5.1.1. Particle data

[39] The particle moments were calculated from the electron electrostatic analyzer (ESA) and ion electrostatic analyzer (IESA) detectors; there is no attempt at mass discrimination. The electron moments were calculated using data from 10 eV to 10 keV, with photoelectron subtraction and with adjustments made for the highly field-aligned quality of the populations. The high-energy cutoff at 10 keV rather than 40 keV was an attempt to reduce the contribution of high-energy precipitation, since the populations under study are the upgoing electrons; thus the moments are not credible in inverted-V precipitation regions where the dominant population has a significant component above 10 keV. Moments and derived quantities calculated include number flux, energy flux, density, parallel temperature, characteristic energy (energy flux/number flux), and characteristic energy restricted to upgoing particles ($\mathcal{E}_{e-}^{up}$). Thermal velocity and bulk flow moments are not reliable, because of the lack of good measurements below 10 eV. For Figures 8, 9, 11, 12, and 15 using electron data, the data set is additionally restricted. The electron characteristic energy calculation is corrupted by the plasma sheet population. To avoid this, data are only used when the pressure-cooker signature is very clear; this is chosen using either where $\mathbf{E}_{\|}^{i}$ is less than −0.02, or where particle fluxes are upward.

[40] The ion moments used were calculated using data from 6 eV up to an upper cutoff energy chosen separately for each crossing. The cutoff energy was chosen to include the upgoing conic populations and exclude the hot ion precipitation. This energy ranges from 1 to 6 keV; there is typically a clear division between the two populations. Occasionally, more than one cutoff would be needed for a given timespan; in this case the event would be broken into two subevents with different cutoffs. Moments and derived quantities include number flux, energy flux, density, parallel temperature, perpendicular temperature, and bulk flow.

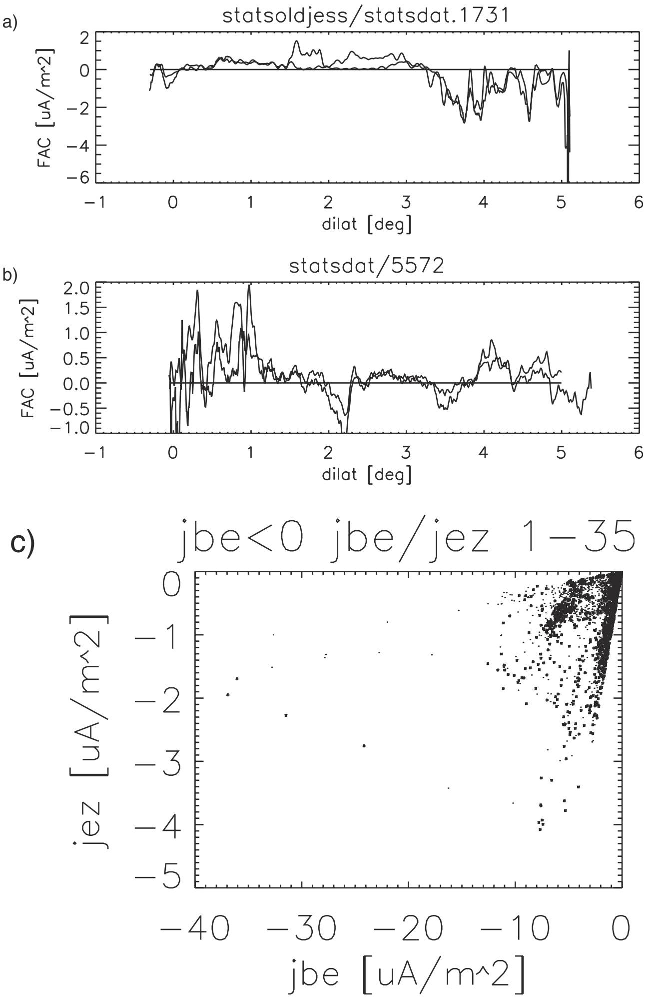

Figure 9. (a, b) Comparison of $\mathbf{j}_z^B$ (thick) and $\mathbf{j}_z^{e-}$ (thin) for two cases, as a function of δ_{ILAT}. (c) A statistical comparison of the two field-aligned current (FAC) calculations. Points and highlighted points are as those in Figure 8.

[41] The ion moments are combined to calculate total ion energy $\mathcal{E}_i$:

$$\mathcal{E}_i = T_{i\perp} + w_{i\parallel},$$

where

$$w_{i\parallel} = \frac{1}{2} m_i u_i^2 + \frac{1}{2} T_{i\parallel},$$

and also to calculate a parallel electric field that is consistent with the observed ion pitch angle distribution, as defined by *Jasperse and Grossbard* [2000] above:

$$\mathbf{E}_{\parallel}^{i} \simeq \frac{2}{e}\frac{1}{B}\frac{\partial B}{\partial s}\left(\frac{1}{2}T_{i\perp} - w_{i\parallel}\right).$$

The superscript on $\mathbf{E}_{\parallel}^{i}$ is a reminder that this parallel field quantity is derived from ion data. Two other particle moment combinations used in the statistical study are (1) the log of the ion temperature ratio, $\log_{10}(T_{i\perp}/T_{i\parallel})$ and (2) the log of the ratio of ion energy to electron characteristic energy (restricted to upgoing electrons), $\log_{10}(\mathcal{E}_i/\mathcal{E}_{e-}{}^{\mathrm{up}})$.

5.1.2. Current data

[42] The field-aligned current is used as a primary sorting quantity for the database and thus needs special care. While the magnetic local time (MLT) is the first selection criterion (events are chosen between 2000 and 0200 MLT), the data that are used from the events that are selected are only the data in the return current regions, that is, regions where the current is downward and electrons go up. (For clarity when dealing with both North and South Pole passes, the sign of the current is designated as positive upward (electrons precipitating) and negative downward (electrons up), rather than as being parallel or antiparallel to **B**. Note that this is different from the convention used for the particle moments, which are signed according to **B**.)

[43] Two methods are used to measure the field-aligned current: one using the electron data and one using the magnetometer data. Current calculated from the electron data is proportional to the number flux moment:

$$\mathbf{j}_z^{e-} = J_{e^-}\left[\mathrm{cm}^{-2}\ \mathrm{s}^{-1}\right] \times e \times 10^4 \times 10^6\left[\mu\mathrm{Am}^{-2}\right].$$

Note that the multiplication is by e, not by $-e$, because of the opposite (Northern Hemisphere) convention for field-aligned current and number flux.

[44] Current calculated from the magnetometer is given by

$$\mathbf{j}_z^{B} = \frac{1}{\mu_o}(\nabla \times \mathbf{B})_z,$$

with the same sign convention as described above. Of course, the single-point FAST measurements do not allow an explicit calculation of $\nabla \times \mathbf{B}$, and an assumption of sheet-like currents needs to be made. A necessary condition, for the validity of the sheet-current assumption, is that $B_{\mathrm{alongtrack}}$ be linearly related to $B_{\mathrm{acrosstrack}}$. When this condition holds, the slope of $B_{\mathrm{alongtrack}}$ versus $B_{\mathrm{acrosstrack}}$ can be used to correct $\partial\mathbf{B}_{\mathrm{alongtrack}}/\partial x$, so that it becomes a reasonable proxy for the current density [*Peria et al.*, 2000].

[45] The two methods can give very different results for $\mathbf{j}_z$. The electron data miss electrons under 10 eV and, if a significant portion of the current is carried by these electrons, typically will underestimate the current density. The magnetometer data require the assumption of a sheet current and a fairly normal-to-the-sheet trajectory. If the currents are not sheet-like (as may often be the case in return-current areas), the curl calculation is flawed. However, when the electron data and the magnetometer data are in reasonable agreement, we can have confidence that the current is being inferred correctly. For the purposes of the statistics below, reasonable agreement is taken to mean

$$1 < \mathbf{j}_z^{B}/\mathbf{j}_z^{e-} < 35.$$

This ensures that $\mathbf{j}_z^{B}$ and $\mathbf{j}_z^{e-}$ are of the same sign, that $\mathbf{j}_z^{B}$ is at least as large as the current measured by the electron detector, and that $\mathbf{j}_z^{B}$ is not spuriously large even if the electron detector is underestimating the current. (Spuriously large $\mathbf{j}_z^{B}$ can result from nongeophysical spikes in the magnetometer data, spacecraft charging effects, and other nongeophysical situations.) If these conditions are met, then $\mathbf{j}_z^{B}$ is used as the measure of $\mathbf{j}_z$.

[46] Figure 9 shows examples of these calculations. Figures 9a and 9b show $\mathbf{j}_z^{B}$ and $\mathbf{j}_z^{e-}$ as a function of δ_{ILAT} for two sample crossings. Figure 9c shows a scatter plot of all the samples meeting the condition $1 < \mathbf{j}_z^{B}/\mathbf{j}_z^{e-} < 35$ for which $\mathbf{j}_z^{B}$ is negative (3416 points). The correlation is positive but not particularly good. The highlighted points are the subset of the data for which the particle energy fluxes are upward (982 points). This subset will be used occasionally below for comparisons that are sensitive to the upward electron energy flux values.

5.1.3. BBELF data

[47] The BBELF quantities included in the database include both integrated spectral density and spectral density at selected frequencies. Data from boom pairs 1–2 (5 m), 1–4 (28.5 m), and 5–8 (55.7 m) are used whenever data up to 2048 samples s^{-1} are available. The data are despun to ($E_\parallel$, $E_\perp$) components in the spin plane, and power spectra are calculated from 4 Hz to 1 kHz with a 1-s time resolution. The spectra are integrated (for integrated spectral density quantities) or sampled (for selected frequencies), and the resulting time series are estimated at the sample times of the particle data by linear interpolation from the original 1-s resolution.

[48] The resulting time series include omnidirectional, parallel, and perpendicular integrated spectral densities for both the 14–58 and the 12–58 sets and omnidirectional and perpendicular spectral density values at $\Omega_{H^+}, \Omega_{He^+},\ and\ \Omega_{O^+}$ for both the 14–58 and 12–58 sets.

[49] A spectral index is calculated from the spectral density values at $\Omega_{H^+}\ and\, \Omega_{O^+}$, idealizing the spectrum as a power law:

$$S(\omega) = S_0\left(\frac{\omega_0}{\omega}\right)^{\alpha},$$

$$\alpha = [\log S(\Omega_{\mathrm{H}^+}) - \log S(\Omega_{\mathrm{O}^+})]/\log\left(\frac{\Omega_{\mathrm{H}^+}}{\Omega_{\mathrm{O}^+}}\right),$$

$$\alpha \equiv \left[\log S_{\perp}^{14-58}(\Omega_{\mathrm{O}^+}) - \log S_{\perp}^{14-58}(\Omega_{\mathrm{H}^+})\right]/1.204.$$

5.1.4. Summary

[50] A summary of the selection criteria for the database is as follows. (1) A total of 90 auroral zone crossings with

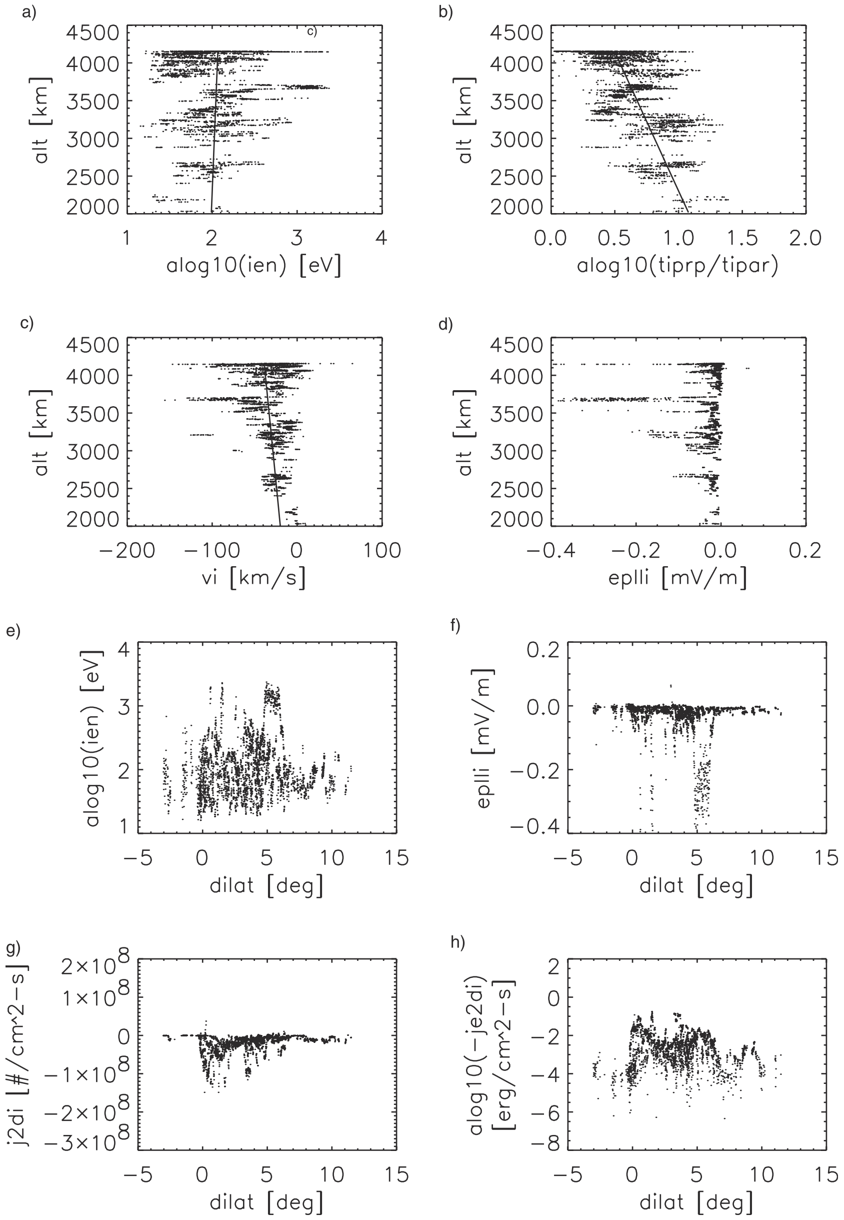

Figure 10. Ion data quantity dependencies on (a–d) altitude and (e–h) δ_{ILAT}. Line traces show average values as functions of altitude.

"pressure-cooker" signatures were chosen. (2) Of these, 23 crossings that met the 2000–0200 MLT restriction and that had ELF data sampled at up to at least 2048 Hz were chosen. (3) Of the 18,060 data samples in this set, 8139 samples had $\mathbf{j}_z^B$ negative (downward current, upward electrons). (4) Of these points, 3416 points met the restrictions for $\mathbf{j}_z^B/\mathbf{j}_z^{e-}$. These are the data samples used for the bulk of the statistical study. (5) Of this set, 982 samples also meet the restriction that the particle energy flux moments are upward. This subset is used for parts of the study. For a database of 3416 samples, correlations are significant (three-sigma) as tested against a null hypothesis if the correlation coefficient r is above 0.05; the error on the correlation coefficients is $\pm(1 - r^2) \times 0.05$. For the database correlations using the smaller set (982 samples), the minimum significant correlation coefficient is 0.1, and the error is $\pm(1 - r^2) \times 0.1$ [*Press et al.*, 1992].

5.2. Results of Statistical Study

5.2.1. Morphology

[51] Figure 10 shows ion data quantities as functions of altitude and δ_{ILAT}. While scatter from activity levels and other variables dominates the plots, certain trends are evident. The average ion energy increases slightly with both altitude and δ_{ILAT}. Certainly, the maximum ion energy increases with altitude, as would be expected. The ion temperature ratio decreases with altitude, as the mirror force moves perpendicular energy into parallel energy. The largest values of the temperature ratio are only ~30; the strong parallel heating is a clear signature that was discussed in section 4 and appears to

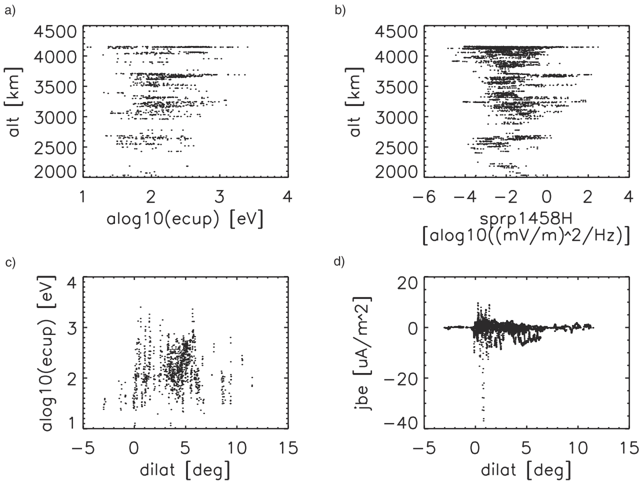

Figure 11. (a, b) Electron characteristic energy (upgoing particles only) and power spectral density at Ω_{H^+} as functions of altitude. (c, d) Electron characteristic energy and field-aligned current density dependencies on $\delta_{\rm ILAT}$. Note that the $\mathbf{j}_z^B$ panel uses data for both positive and negative $\mathbf{j}_z^B$, unlike all the other panels, which are restricted to negative $\mathbf{j}_z^B$.

be related to relatively slow perpendicular heating rates. The average ion bulk velocity ranges from ~20 km s^{-1} at 2000-km altitude to ~50 km s^{-1} at 4000-km altitude. This implies a typical ion conic "lifetime," below 4000-km altitude, of the 3000-km range to the ionospheric source, divided by the 35 km s^{-1} speed, or 85 s. If typical ion energies at 4000-km altitude are 100 eV to 1 keV, this implies a typical average heating rate of only ~1–10 eV s^{-1}.

[52] Figure 10 also shows ion-data-inferred local parallel electric fields $\mathbf{E}_\|^i$, as functions of altitude and $\delta_{\rm ILAT}$. No clear dependencies are seen other than cutoffs below 2500-km altitude and 0° $\delta_{\rm ILAT}$, but the range of values is comparable to that of the altitude profiles used in section 4.

[53] Ion number flux and energy flux show dependencies on $\delta_{\rm ILAT}$, with maximum values nearest the polar cap edge. Note that the number flux plot has a linear vertical axis and upward number fluxes are negative (antiparallel to **B**), while the energy flux plot has a logarithmic vertical axis and only shows points for samples with upward (negative) energy flux.

[54] Figure 11 shows electron, wave, and current dependencies on $\delta_{\rm ILAT}$ and altitude. The characteristic energy of the upgoing electron population ($\mathcal{E}_{e-}^{\rm up}$) is highly variable and shows only a slight increase over the available altitude range. Note that the electron data plots, as discussed above, are restricted to times of strong pressure-cooker signatures. The power spectral density at the local hydrogen gyrofrequency shows no altitude dependence, although the integrated power over the 4 Hz to 1 kHz band (not shown) shows a slight increase. The spectral index (not shown here) has no discernible altitude or $\delta_{\rm ILAT}$ trend.

[55] Figure 11d shows the field-aligned current density as a function of $\delta_{\rm ILAT}$. Note that this panel, unlike the others, includes both positive and negative values of $\mathbf{j}_z^B$. There is a region of intense and variable current densities near the poleward edge, and a subsequent falling off of current density with increasing $\delta_{\rm ILAT}$.

5.2.2. Relationships

[56] Having examined the various morphological trends, we can now turn to the relationships between the various data quantities. Figure 12 shows several comparisons. The ion energy ranges from ~1 to 10 times the electron characteristic energy (upgoing). (Again, note the restriction on the available electron data to times of clear pressure-cooker signatures.) There is no clear altitude or $\delta_{\rm ILAT}$ dependence of $\mathcal{E}_i/\mathcal{E}_{e-}^{\rm up}$. The ion temperature ratio reaches its highest values when the ELF spectrum is hardest (smallest index value). However, a hard spectrum does not guarantee a high temperature ratio, because while the spectral index is local to the measurement, the temperature ratio is a cumulative parameter and depends on the history of the ion population as it moves up the field line.

[57] We begin to find better correlations when we compare the ion energy to the local power spectral density or to the strength of the current density. These values are better indicators of general activity levels on the entire field line and are better matched to the accumulation of ion energy below and up to the measurement point.

[58] A better parameter than $\mathcal{E}_i$ for comparison with local measurements is the parallel electric field inferred from the ion pitch angle distribution. While $\mathcal{E}_i$ is a cumulative parameter, $\mathbf{E}_\|^i$ is the parallel field that is consistent with the pitch angle distribution at the point of the measurement. Figure 13 compares local wave field parameters to local observations of parallel electric field ($\mathbf{E}_\|^i$ from the ion data) and field-aligned current density ($\mathbf{j}_z^B$ from the magnetometer). While the spectral index still is not well correlated with either parameter, the power spectral density is somewhat correlated with both.

5.2.3. Correlations

[59] When we compare the power spectral density to the product of the field-aligned current density and the locally inferred parallel electric field, we find the strongest correla-

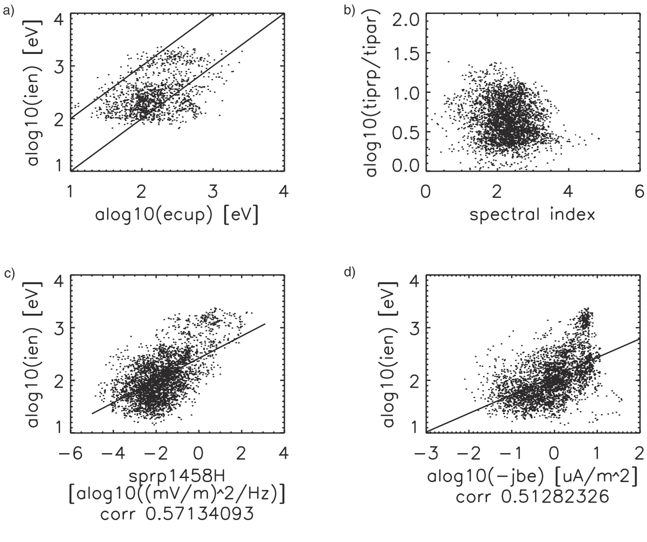

Figure 12. (a–d) Relationships between ion and electron energies, ion temperature ratios and wave field parameters, and field-aligned current density. Straight lines in Figure 12a show $y = x$ and $y = 10x$. Lines in Figures 12c and 12d are best fit least squares regression lines; correlation coefficients are shown in the subtitles.

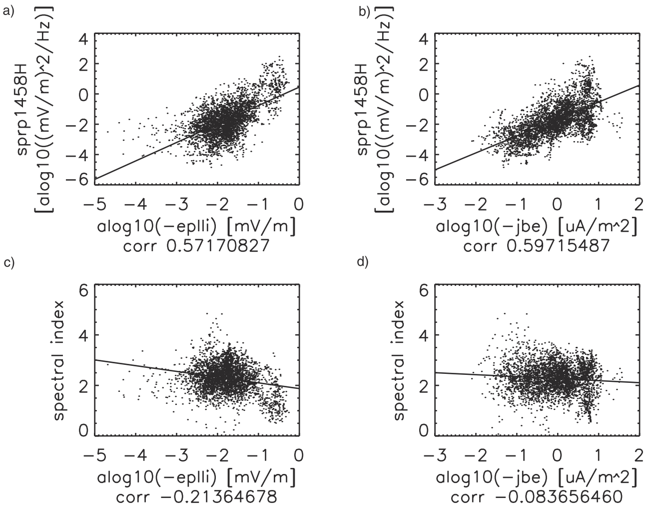

Figure 13. Dependence of wave field parameters on local parallel electric field and field-aligned current density. Straight lines are best fit linear regressions; correlation coefficients are shown in the subtitles.

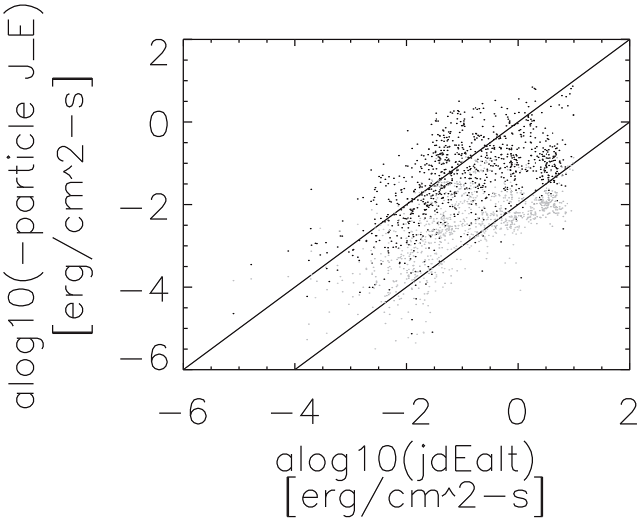

Figure 15. Particle energy fluxes versus DC input. Black dots are electron energy flux (upward) values; red dots are ion energy flux (upward) values. Diagonal lines are traces of $y = x$ and $y = x/100$.

tion. Figure 14 shows these relationships. The quantity $\mathbf{j}_z \cdot \mathbf{E}_\|$ is the power dissipated per unit volume by the coexistence of a downward field-aligned current and a downward electric field, where the current is measured by the magnetometer and the field is inferred from the ion moments:

$$\mathbf{j}_z \cdot \mathbf{E}_\| = \mathbf{j}_z^B \cdot \mathbf{E}_\|^i \left[\mathrm{erg\ cm^{-3} s^{-1}}\right].$$

The two panels of Figure 14 show the integrated BBELF wave power (left) and the wave power at only Ω_{O^+} (right), as functions of the DC power input $\mathbf{j}_z \cdot \mathbf{E}_\|$. The correlation coefficient of the right panel is 0.71, which is remarkable given the varied data sources of the plot. This panel should be compared to Figure 6, which shows the same relationship but for a single auroral pass (wherein the correlation coefficient is 0.85).

[60] The wave power spectral density is therefore positively correlated with the ion energy ($r = 0.57$), the parallel field ($r = 0.57$), and the field-aligned current ($r = 0.60$), but it is significantly better correlated ($r = 0.71 \pm 0.02$) with power dissipation as measured by the quantity $\mathbf{j}_z \cdot \mathbf{E}_\|$.

5.2.4. Energy flow

[61] We can compare the DC input power from $\mathbf{j}_z \cdot \mathbf{E}_\|$ to the particle energy fluxes coming up out of the flux tube below the measurement. If we assume that the power dissipation from $\mathbf{j}_z \cdot \mathbf{E}_\|$ is independent of altitude down to 1000 km (a plot of $\mathbf{j}_z^B \cdot \mathbf{E}_\|^i$ versus altitude shows no clear trend), then we can multiply $\mathbf{j}_z \cdot \mathbf{E}_\|$ times the length of the field line below the observation to find the energy being pumped into the flux tube below the observation:

$$\int \mathbf{j}_z \cdot \mathbf{E}_\| ds = \mathbf{j}_z \cdot \mathbf{E}_\|^i \times L\left[\mathrm{erg\,cm^{-2}\ s^{-1}}\right].$$

This quantity can be compared numerically to the energy flux leaving the flux tube being carried by the ion and electrons, the energy fluxes J_E. Figure 15 shows this comparison. The black dots show the (upgoing) energy flux

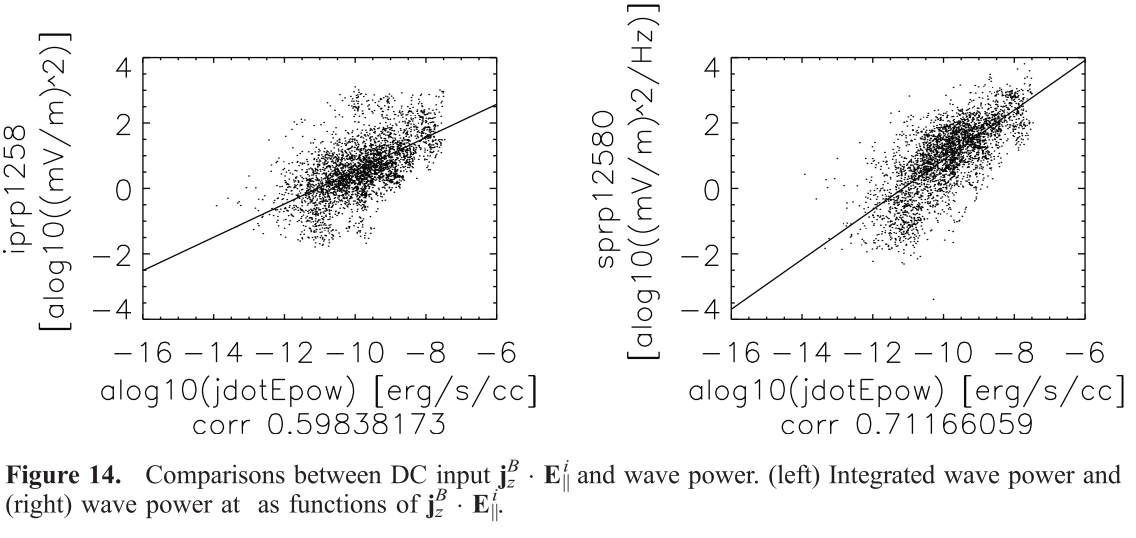

Figure 14. Comparisons between DC input $\mathbf{j}_z^B \cdot \mathbf{E}_\|^i$ and wave power. (left) Integrated wave power and (right) wave power at as functions of $\mathbf{j}_z^B \cdot \mathbf{E}_\|^i$.

Table 1. Correlations Between Wave Power, $\mathbf{j}_z \cdot \mathbf{E}_\parallel$, and Particle Energy Fluxes[a]

	J_E, e^-	$J_{E,\ \mathrm{ions}}$	S,Ω_{O^+}
$\mathbf{j}_z^B \cdot \mathbf{E}_\parallel^i$	0.58 ± 0.07	0.63 ± 0.06	0.71 ± 0.02
J_E, e^-		0.63 ± 0.06	0.62 ± 0.06
J_E,ions			0.62 ± 0.06

[a] All quantities are logarithms.

of electrons; the green dots show the energy flux of ions. The diagonal traces are lines of $y = x$ and $y = x/100$. The electron energy flux is comparable to the DC power input; the ion energy flux is ~10%.

[62] Under the assumption that the electrons gain their energy directly from the DC electric field but that the ions gain their energy from the ELF wave field (which is generated from the dissipation of $\mathbf{j}_z \cdot \mathbf{E}_\parallel$, through thermalization of the resulting accelerated electrons), it is interesting to compare the wave power to the particle energy fluxes. The ion heating continually removes energy from the wave field, and the electron thermalization continually feeds energy to the wave field, but neither of these processes would set the level of wave activity, so it is interesting that the wave power should be so well correlated with the input $\mathbf{j}_z \cdot \mathbf{E}_\parallel$ power. We can consider the correlations between each of these parameters. Table 1 shows the correlations between $\mathbf{j}_z \cdot \mathbf{E}_\parallel$, particle energy fluxes, and local wave power $S(\Omega_{O^+})$ using the statistical database restricted further to cases when the particle energy fluxes are upward (982 samples), except for the $\left(j_z \cdot E_\parallel,\ S(\Omega_{O^+})\right)$ case, which does not involve particle fluxes. The strongest correlation is the one pointed out just above, between the wave activity and the DC power input. This correlation is stronger than that between the wave activity and either the upgoing ion or electron energy flux, and it is stronger than that between the ion energy flux and the DC power input (which is artificially enhanced by the fact that both quantities use the ion data.)

[63] The relative strengths of the correlations indicate that the wave activity is locally dependent on the DC power input, while the particle acceleration proceeds on a more slowly varying timescale over the entire length of the flux tube, reducing the correlation with the local rate of energy input. Note, however, that all the parameters are moderately well correlated, and the entire system seems to find a local equilibrium fairly quickly.

5.2.5. Energy density

[64] Another way of comparing the ion energization to the wave field is to consider the energy density at each altitude rather than the energy flux out the top. Figure 16 shows an altitude profile of ion energy density, together with one of ion number density for reference.

[65] In order to understand whether the observed wave activity is a sufficient energy source for the heated ions, we can assume a cyclotron resonant heating mechanism and calculate the possible ion energies allowable from the waves. This was done by *André et al.* [1998] and *Knudsen et al.* [1998] for Freja data using a theoretical energy transfer given by *Chang et al.* [1986]:

$$\frac{dW}{dt} = S_L(\Omega_{ci})q^2/(2m_i),$$

where S_L is the spectral density of left-hand-polarized waves at the ion cyclotron frequency. Figure 17 shows the results of a similar calculation for the FAST data. The bottom plots show the maximum possible cyclotron heating rate (assuming 100% left-hand polarization and 100% wave absorption) for oxygen and hydrogen given the observed spectral densities as a function of altitude over the available statistics. The oxygen heating rate is normally well above the nominal necessary 1 eV s^{-1}, but the hydrogen is not. We can estimate the attainable ion energies from these heating rates by using the observed ion bulk flow moment to calculate the upward velocity of the ions. Assuming that all ions start at 1000 km, then the lifetime of the ion conic up to the point of observation is approximately

$$t = (\mathrm{altitude} - 1000.)/(0.5\, v_{\mathrm{bulk}}).$$

Then the cyclotron resonant heating could provide ion energies of $t \times dW/dt$, given that S_L at the observation point is indicative of power at Ω_{ci} all along the flux tube. This would appear a fair assumption given the lack of altitude dependence of the wave spectral density shown in Figure 11. Figures 17a and 17b compare the observed ion energies to the cyclotron resonant obtainable energies, as a function of $S(\Omega_{ci})$. The dots are the observed energies, and the red dots are the calculated possible energies. If all the ions were oxygen, there would appear to be sufficient wave power. However, they are not, and moreover, the typical ion energies in the pressure-cooker regions are not mass-dependent [*Lund et al.*, 1999], that is, hydrogen and oxygen energies within a given event are generally comparable within a factor of 2.

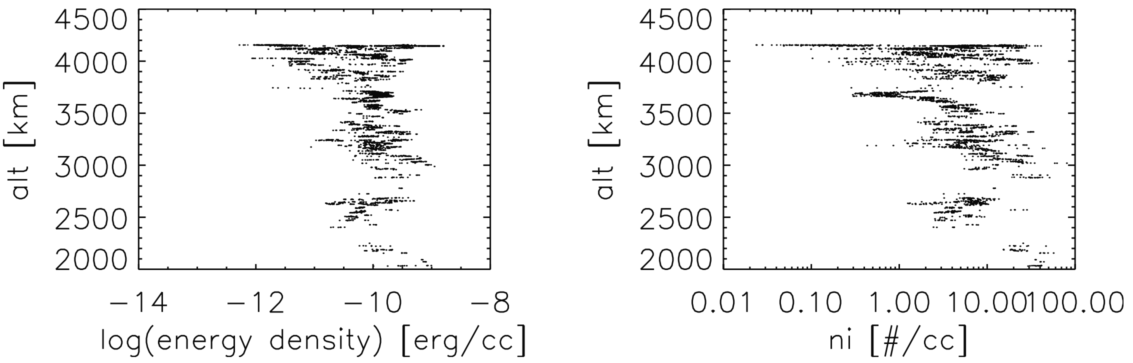

Figure 16. Altitude profiles of ion energy density and ion number density.

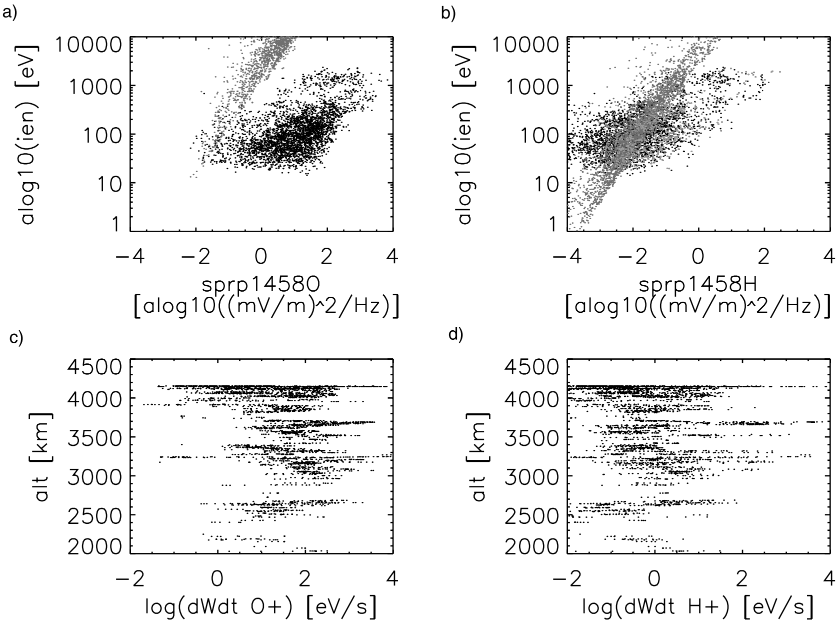

Figure 17. (a, b) Observed ion energies (black dots) and possible cyclotron heating (red dots) and (c, d) heating rates as in Freja study [*André et al.*, 1998]. Green dots in Figure 17b events near the polar cap edge.

[66] We can make a crude mass discrimination of the IESA statistics by using the information that the events very near the polar cap edge are mostly hydrogen [*Tung et al.*, 2001]. If we restrict our statistics to events within 2° of the polar cap edge, the difficulty with the hydrogen heating is somewhat lessened. The green dots overlaid on Figure 17b show observed ion energies for these most poleward events; the bulk of these events are at energies less than the maximum available from the hydrogen heating.

5.2.6. Current-Voltage relations

[67] Having seen that the wave field power and the particle energy fluxes are controlled by neither the field-aligned current, nor the electric field strength, but by their product, $\mathbf{j}_z \cdot \mathbf{E}_{\|}$, we next turn to the question of what controls the relationship between the (externally controlled) field-aligned current density and the (internal response) parallel electric field strength. Figure 18 shows why the morphology of the "pressure-cooker" regions appears to be controlled by the distance from the polar cap edge. The δ_{ILAT} dependence is really a dependence on local particle density, and it is the particle density that controls, for a given field-aligned current density, the amount of parallel field that forms to meet that current requirement.

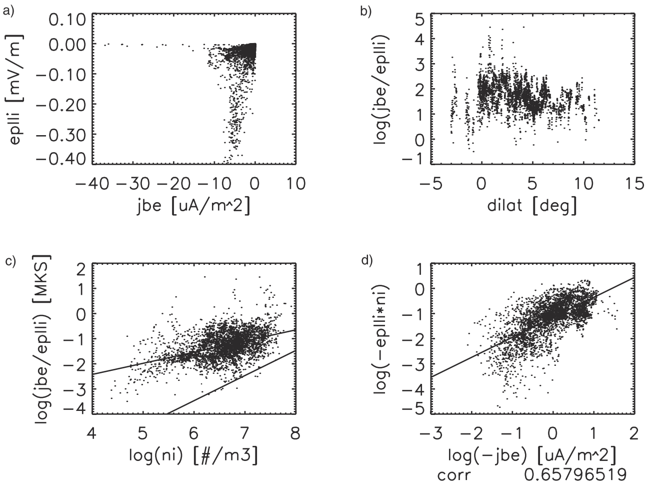

Figure 18. (a–d) $\mathbf{E}_{\|}$, $\mathbf{j}_z$ relationship; dependence on n_i (δ_{ILAT}).

[68] Figure 18a is a scatterplot of $\mathbf{E}_{\|}^i$ as a function of $\mathbf{j}_z^B$. Clearly, there is no single expected $\mathbf{E}_{\|}^i$ for a given value of $\mathbf{j}_z^B$. Figure 18b shows that the ratio of $\mathbf{j}_z^B$ to $\mathbf{E}_{\|}^i$ is a function of δ_{ILAT}. Near the polar cap edge, the $\mathbf{j}_z$ requirement is met with a small $\mathbf{E}_{\|}$, so the ratio is large. Moving away from the edge, a given $\mathbf{j}_z$ requires stronger and stronger $\mathbf{E}_{\|}$, so the ratio decreases. The dominant morphological signature of δ_{ILAT} is the decreasing density as the auroral density cavity is entered; n_i is large near the polar cap edge and decreases with increasing δ_{ILAT}. Thus we can recast the (morphological) Figure 18b as a dependence of $\mathbf{j}_z^B/\mathbf{E}_{\|}^i$ on n_i; this is shown in Figure 18c. (The two straight lines on this plot will be discussed in section 6.1, below.) For small n_i the external $\mathbf{j}_z$ requirement is met with a large $\mathbf{E}_{\|}$; as the density increases, less and less $\mathbf{E}_{\|}$ is necessary. Finally, in Figure 18d we recast this plot once again, with ion detector data derived quantities on the y-axis, and magnetometer-derived quantities on the x-axis, to find a correlation coefficient of 0.66.

6. Discussion

[69] The data presentation in this paper is motivated by several goals. One straightforward goal is simply to lay out the observed parameters of ion heating in reverse aurora for the use of modelers and theorists working on the problem of electric field formation in these regions. A second goal is to explore the range of applicability of a simple pressure-cooker model to the auroral zone. We find that it applies to a wide range of auroral regions, including strong return-current regions and also poleward edge regions where the

parallel fields are small. A third goal is to examine the observed energy densities and energy fluxes of the various parameters for discussions of causality and energy flow and as a basis for ongoing and future studies of BBELF formation in these regions. Our first goal has been met in section 5; we consider the second and third goals below.

6.1. Formation of $\mathbf{E}_{\|}$ to Satisfy Externally Required $\mathbf{j}_z$

[70] Premidnight auroral regions can be categorized in many ways. The simplest division is (1) inverted-V regions and (2) everything else. Within group 2, there are regions which are clear reverse aurora, with strong downward currents and fields, and there are regions, particularly near the polar cap edge, where the currents and fields can be either oscillating or weak. The morphologies of the strong reverse aurora regions and of the polar cap edge regions look very different from each other if one considers number density or particle fluxes. The polar cap edge regions are characterized by a strong number flux outflow of hydrogen (see Figure 10 and *Tung et al.* [2001].) The strong reverse aurora regions have a mixed outflow of equal energy hydrogen and oxygen and are characterized by their strong downward currents and fields. However, the simple pressure-cooker model appears to cover the processes occurring in both cases, although with different parameters.

[71] In Figure 18 we can see that the relationship between the (presumably externally defined) parallel current, and the (presumably resulting) parallel electric field is controlled by the number density of the ions. This observational result bears out the theoretical description given by *Temerin and Carlson* [1998] that the ionospheric density, as affected by the pressure-cooker heating process, has a feedback effect on the strength of the parallel electric field. Thus, in the center of the auroral cavity, where the ionospheric density is low, strong parallel fields are needed to pull out the requisite number of upgoing electrons to meet the current requirement. These strong fields generate strong pressure-cooker ion heating. Near the edges of the auroral cavity, where the ionospheric density is high, only weak parallel fields are needed for the same electron current. The weak fields generate minimally visible pressure-cooker signatures in the ion distributions.

[72] The statistics shown in Figure 18 could be ordered better by controlling for the plasma sheet electron temperature, which also affects $\mathbf{E}_{\|}$ as described by *Temerin and Carlson* [1998]. The electric field formation is a balance between the densities of the various populations. (We note in passing that in all the cases used in this study, there was a hot precipitating ion population, thus Type 2 of *André et al.* [1998]. The temperature and density of the plasma sheet population of electrons and ions (visible in Figure 2) also have an effect in controlling the strength of the parallel field for a given current requirement; this effect is not considered here, and we only measure the effect of varying the ionospheric populations.

[73] We can view the results shown in Figure 18 as a measure of the effective conductivity of the wave activity on the field line. If $\mathbf{j}_z = \sigma\mathbf{E}_{\|}$, then the ratio $\mathbf{j}_z/\mathbf{E}_{\|}$ is a measure of effective conductivity. Note that given the derivation of $\mathbf{E}_{\|}^i$ used here, the parallel field is supported not by a collisional or even anomalous collisional resistivity but rather by the wave-particle ion heating that produces velocity diffusion in the ion distribution function. Thus the relationship between $\mathbf{j}_z$ and $\mathbf{E}_{\|}$ is not directly that of a resistance or conductivity σ but rather an indirect relationship covering many processes.

[74] Figure 18c includes two lines: the upper line is a best fit linear regression to the data points. We see that the observed relationship between $\mathbf{j}_z$ and $\mathbf{E}_{\|}^i$ is roughly that of $\sqrt{n}$. In order to put this effective conductivity in perspective, we include a calculation of a more standard conductivity, that from the anomalous resistivity of ion-cyclotron wave activity. The lower line in Figure 18c is a calculation of the minimal possible conductivity (highest anomalous resistivity) given a hypothesis of anomalous resistivity from ion-cyclotron collisions. The effective collision frequency in this case is of the order of the ion gyrofrequency [*Treumann and Baumjohann*, 1997], and thus the conductivity can be calculated as

$$\sigma_{ion-cyc} = \varepsilon_o \omega_{pe}^2 \Big/ \nu_{ion-cyc},$$

$$\nu_{ion-cyc} \approx \Omega_{ci},$$

$$\sigma_{ion-cyc} = \varepsilon_o \omega_{pe}^2 \Big/ \Omega_{ci} = \frac{e}{B} \frac{m_i}{m_e} n.$$

[75] This discussion is not meant to show that ion-cyclotron-like waves are causing resistance on the field lines but rather to show that (1) the effective conductivity remains higher than that possible from anomalous ion-cyclotron resistance and that (2) the effective conductivity approaches that of $\sigma_{ion\text{-}cyc}$ at higher densities. These data should give a reference point for possible explanations of the structure of BBELF.

6.2. Dissipation of $\mathbf{j}_z \cdot \mathbf{E}_{\|}$ Into Wave Growth and Particle Energization

[76] The energy source for the ion heating appears to be the wave growth generated by the power dissipation required by the coexistence of the downward parallel current and the downward parallel electric field. The wave growth thermalizes the electron beam and also heats the ion population, allowing the ion density to move up and maintain quasi-neutrality. The ion heating thus tends to somewhat suppress the parallel field strength, as noted by *Temerin and Carlson* [1998], as it increases the local ionospheric density (and scale height.)

[77] We note in passing, though this topic is beyond the scope of this paper, that the relationship between $\mathbf{j}_z \cdot \mathbf{E}_{\|}$ and the BBELF intensity appears to hold true in the inverted-V regions as well. When FAST is within the parallel field region of an inverted-V structure, as indicated by the presence of ion beams, the coexistence of the upward field and the upward current again is manifested as a power dissipation that is matched by the local BBELF intensity. (See Figure 2 for two examples.) This process invariance between different regions may be an important clue in determining the source of BBELF generation.

6.3. Structuring Within Return Current Regions

[78] Finally, we touch on another interesting aspect of these regions. The typical ion conic transit time from 1000 to 4000 km is ~85 s. The typical electron transit time is a fraction of a second. A typical FAST horizontal transit of return current region is ~30 s. Thus the FAST energy-time spectrogram for the electrons shows the instantaneous

behavior of the potential drop below the spacecraft throughout the crossing. However, the energy-time spectrogram for the ions shows effects integrated over any rapid time variations. For many examples [*Ergun et al.*, 1998a] the return-current potential structures are spatially rather than temporally structured on the timescale of the FAST crossing, as evidenced by matching the electron characteristic energies with the integrated perpendicular electric field. For other examples [*Chaston et al.*, 2001] the upgoing electrons are part of Alfvénic structures, and the electric field can be assumed to be time varying on the timescale of the FAST crossing. In all cases the strong perpendicular fields imply strong perpendicular flows, and this can be seen often in the nongyrotropic nature of many of the ion distributions. Thus it is reasonable to consider the possibility that the ion distribution observed at satellite altitudes may have evolved with a electric field profile that varied over the lifetime of the ion conic. Running the simple test particle model with a time-varying potential structure has the effect that the ion to electron energy ratio is somewhat lowered. This is a subject for further study, but there is some evidence that this may be happening in the FAST data, as the ion to electron energy ratio has a slight trend to decrease near the poleward edge, where the fields are more likely to be time varying.

7. Conclusions

[79] In this paper we have considered ion heating in downward current, downward electric field, premidnight auroral regions. We showed a case study, a test particle model, and a statistical study. The case study and statistical study use electron, ion, wave, and field-aligned current data and include wave spectra and ion pitch angle distributions. The ion pitch angle distribution functions are used to calculate, through the momentum balance equation, a self-consistent local parallel electric field. The test particle model shows ion pitch angle distributions and moments resulting from a "pressure-cooker" arrangement of magnetic and electric fields. The statistical database uses data from 23 premidnight auroral FAST crossings.

[80] The statistical study shows that the ion to electron energy ratio varies from 1 to 10; the BBELF wave power is controlled by the local value of $\mathbf{j}_z \cdot \mathbf{E}_\parallel$; the relationship between $\mathbf{j}_z$ and $\mathbf{E}_\parallel$ is controlled by n_i; and the wave power near the cyclotron frequency is sufficient to provide the observed ion energies for oxygen in all cases, and the observed ion energies for hydrogen for events near the poleward edge. The strong correlation between the wave power and $\mathbf{j}_z \cdot \mathbf{E}_\parallel$ validates the use of the ion distributions as a probe of the local $\mathbf{E}_\parallel$.

[81] The simple test particle model can reproduce the ion pitch angle distributions and the moments of these distributions as seen in the statistical database. Modifying the test particle model to allow time-varying electric fields has the net effect of reducing the ion to electron energy ratio, but the statistics (particularly the electron data) are insufficient at present to verify a need for this time dependence.

[82] As expected from theoretical arguments, the current-voltage relationship in these regions is seen to be controlled by the local ionospheric density. Allowing for a suitable range in values of the density, the model can be applied to both strong return-current regions within the auroral cavity and weak-field regions at the poleward boundary.

[83] The results from this initial statistical survey invite a host of further studies. A short list of parameters that should be added to the database includes (1) plasma sheet temperature as measured by the high-energy precipitation, (2) some indication of ion conic mass, and (3) further BBELF parameters, particularly an index of spatial irregularities as derived from coherency studies. In addition, we note that the present database tends to underestimate strong high-energy conics, as they reach energies that merge with the precipitating plasma sheet population; a specific study of these high-energy events should also prove interesting. Many of the high-energy events are strongly nongyrotropic; a comparison of these data with perpendicular DC electric field data can be part of a study of the spatial irregularities in the wave fields.

[84] **Acknowledgments.** The authors gratefully acknowledge productive conversations with J. Jasperse regarding the theory of parallel electric field formation and particle distribution signatures. In addition, we thank Eric Lund and Mats Andre for their input. As with any study using the FAST data set, we are heavily dependent upon the entire FAST team, particularly including support for the extensive software library. This particular study was funded by the NASA Guest Investigator program under NASA grant NAG5-7798 and by the FAST MO/DA grant NAG-3596. UNH undergraduate student Jessica Ward assisted with the building of the statistical database.

[85] Hiroshi Matsumoto thanks J. R. Jasperse and R. Fujii for their assistance in evaluating this paper.

References

Alfvén, H., and C. G. Falthammar, *Cosmical Electrodynamics*, Oxford Univ. Press, New York, 1963.

André, M., P. Norqvist, L. Andersson, L. Eliasson, A. Eriksson, L. Blomberg, R. Erlandson, and J. Waldemark, Ion energization mechanisms at 1700 km in the auroral region, *J. Geophys. Res.*, *103*, 4199, 1998.

Boehm, M. H., J. Clemmons, J. E. Wahlund, A. Eriksson, L. Eliasson, L. Blomberg, P. Kintner, and H. Hofner, Observations of an upward directed electron beam with the perpendicular temperature of the cold ionosphere, *Geophys. Res. Lett.*, *22*, 2103, 1995.

Bonnell, J., P. M. Kintner, J. E. Wahlund, K. A. Lynch, and R. L. Arnoldy, Interferometric determination of broadband ELF wave phase velocity within a region of transverse ion acceleration, *Geophys. Res. Lett.*, *23*, 3297, 1996.

Carlson, C. W., et al., FAST observations in the downward auroral current region: Energetic upgoing electron beams, parallel potential drops, and ion heating, *Geophys. Res. Lett.*, *25*, 2017, 1998.

Cattell, C. A., et al., The association of electrostatic ion cyclotron waves, ion and electron beams and field-aligned currents: FAST observations of an auroral zone crossing near midnight, *Geophys. Res. Lett.*, *25*, 2053, 1998.

Chang, T., G. B. Crew, N. Herkowitz, J. R. Jasperse, J. M. Retterer, and J. D. Winningham, Transverse acceleration of oxygen ions by electromagnetic ion cyclotron resonance with broad band left-hand polarized waves, *Geophys. Res. Lett.*, *13*, 636, 1986.

Chaston, C. C., W. J. Peria, C. W. Carlson, R. E. Ergun, and J. P. McFadden, FAST observations of inertial Alfvén waves and electron acceleration in the dayside aurora, *Phys. Chem. Earth*, *26*, 201, 2001.

Ergun, R. E., et al., FAST satellite observations of electric field structures in the auroral zone, *Geophys. Res. Lett.*, *25*, 2025, 1998a.

Ergun, R. E., et al., FAST satellite observations of large-amplitude solitary structures, *Geophys. Res. Lett.*, *25*, 2041, 1998b.

Gorney, D. J., Y. T. Chiu, and D. R. Croley, Trapping of ion conics by downward parallel electric fields, *J. Geophys. Res.*, *90*, 4205, 1985.

Hultqvist, B., On the acceleration of positive ions by high-altitude, large-amplitude electric field fluctuations, *J. Geophys. Res.*, *101*, 27,111, 1996.

Jasperse, J. R., Ion heating, electron acceleration, and the self-consistent parallel *E*-field in downward auroral current regions, *Geophys. Res. Lett.*, *25*, 3485, 1998.

Jasperse, J. R., and N. Grossbard, The Alfvén-Falthammar formula for the parallel *E* field and its analogue in downward auroral-current regions, *IEEE Trans. Plasma Sci.*, *28*, 1874, 2000.

Kindel, J. M., and C. F. Kennel, Topside current instabilities, *J. Geophys. Res.*, *76*, 3055, 1971.

Kintner, P. M., J. Bonnell, R. Arnoldy, K. Lynch, C. Pollock, and T. Moore, Scifer - transverse ion acceleration and plasma waves, *Geophys. Res. Lett.*, *23*, 1873, 1996.

Knudsen, D., J. Clemmons, and J. Wahlund, Correlation between core ion energization, suprathermal electron bursts, and broadband ELF plasma waves, *J. Geophys. Res.*, *103*, 4171, 1998.

Lund, E. J., E. Mobius, R. E. Ergun, and C. W. Carlson, Mass-dependent effects in ion conic production: The role of parallel electric fields, *Geophys. Res. Lett.*, *26*, 3593, 1999.

Lundin, R., and L. Eliasson, Auroral energization processes, *Ann. Geophys.*, *9*, 202, 1991.

Lynch, K. A., R. L. Arnoldy, J. Bonnell, and P. M. Kintner, The AMICIST auroral sounding rocket: A comparison of transverse ion acceleration methods, *Geophys. Res. Lett.*, *23*, 3293, 1996.

Marklund, G., L. Blomberg, C. Falthammar, and P. Lindqvist, On intense diverging electric fields associated with black aurora, *Geophys. Res. Lett.*, *21*, 1859, 1994.

McFadden, J. P., et al., Spatial structure and gradients of ion beams observed by FAST, *Geophys. Res. Lett.*, *25*, 2021, 1998.

Miyake, W., T. Mukai, and N. Kaka, On the evolution of ion conics along the field line from EXOS D observations, *J. Geophys. Res.*, *98*, 11,127, 1993.

Norqvist, P., M. Andre, and M. Tyrland, A statistical study of ion energization mechanisms in the auroral region, *J. Geophys. Res.*, *103*, 23,459, 1998.

Peria, W. J., C. Carlson, R. Ergun, J. McFadden, J. Bonnell, R. Elphic, and R. Strangeway, Characteristics of field-aligned currents near the auroral acceleration region: FAST observations, in *Magnetospheric Current Systems*, *Geophys. Monogr. Ser.*, vol. 118, edited by S.-I. Ontani et al., p. 181, AGU, Washington, DC, 2000.

Press, W. H., S. A. Teukolsky, W. T. Vetterling, and B. P. Flannery, *Numerical Recipes in C*, 2nd ed., Cambridge Univ. Press, New York, 1992.

Temerin, M., and C. W. Carlson, Current-voltage relationship in the downward auroral current region, *Geophys. Res. Lett.*, *25*, 2365, 1998.

Temerin, M., J. McFadden, M. Boehm, C. W. Carlson, and W. Lotko, Production of flickering aurora and field-aligned electron flux by electromagnetic ion cyclotron waves, *J. Geophys. Res.*, *91*, 5769, 1986.

Treumann, R., and W. Baumjohann, *Advanced Space Plasma Physics*, Imperial Coll. Press, London, 1997.

Tung, Y.-K., C. W. Carlson, J. P. McFadden, D. M. Klumpar, G. K. Parks, W. J. Peria, and K. Liou, Auroral polar cap boundary ion conic outflow observed on FAST, *J. Geophys. Res.*, *106*, 3603, 2001.

J. W. Bonnell and C. W. Carlson, Space Sciences Laboratory, University of California, Berkeley, CA 94720, USA. (jbonnell@ssl.berkeley.edu)

K. A. Lynch, Institute for the Study of Earth Oceans and Space, University of New Hampshire, Durham, NH 03824, USA. (kristina.lynch@unh.edu)

W. J. Peria, Geophysics Program, University of Washington, Seattle, WA 98195, USA. (peria@geophys.washington.edu)